Dynamical Forcing of Stratospheric Planetary Waves by Tropospheric Baroclinic Eddies

J. F. SCINOCCA* AND P. H. HAYNES

Centre for Atmospheric Science,+ Department of Applied Mathematics and Theoretical Physics, University of Cambridge, Cambridge, United Kingdom

(Manuscript received 10 March 1997, in final form 6 November 1997)

ABSTRACT

The forcing of planetary wave variability in the stratosphere by synoptic-scale baroclinic eddies in the troposphere is considered. Simple forced–dissipative numerical experiments are performed in a primitive equation model using a deep hemispheric model domain. The flow is thermally relaxed toward zonally symmetric notional wintertime conditions. No zonally asymmetric thermal or topographic forcing is applied. All planetary-scale zonal asymmetry arises solely through the nonlinear wave–wave interaction of the baroclinic eddies in the troposphere. The numerical experiments indicate that realistic stratospheric planetary wave amplitudes and variability, comparable to those observed in the Southern Hemisphere, can be forced through this mechanism. No evidence is found in these simulations for planetary-scale disturbances arising through in situ instability in the stratosphere.

The nonlinear tropospheric forcing mechanism in the numerical simulations is further investigated by reproducing the stratospheric planetary wave response with a linear model that is forced by the nonlinear eddy forcing that acted in the troposphere of the nonlinear simulation. The forced linear model experiments indicate that (i) as anticipated, both the eddy vorticity forcing and the eddy temperature forcing are required to account for the planetary wave response, (ii) only the low-frequency component of the nonlinear forcing is important, (iii) the vertical structure of the eddy forcing is equivalent to a compact source near tropopause level, and (iv) the variability of the planetary wave response in the stratosphere arises primarily from the variability of the nonlinear eddy forcing in the troposphere, rather than from the variability of the wave propagation characteristics associated with the basic-state zonally averaged flow.

The eddy vorticity and eddy temperature forcing fields are combined into a single expression by introducing a transformation of the equations that govern the Fourier decomposition of deviations away from the zonally averaged flow, referred to as the transformed Fourier decomposition (TFD). The TFD transformation is essentially a generalization of that used in the transformed Eulerian mean formalism. The spatial and temporal characteristics of the total eddy forcing are then analyzed.

The baroclinic eddies in the troposphere of the full simulation show strong organization into wave packets with a dominant wave-2 structure in amplitude. There is a strong, high-frequency, nonlinear wave-2 forcing associated with these packets. However, the propagation characteristics of the background flow in the simulation do not allow upward propagation of wave-2 disturbances with the corresponding frequency and there is little associated signal in the stratosphere. Experiments with a linear model, applying the same nonlinear forcing, show that there are background zonal flows, with plausibly realistic velocity fields, that allow upward propagation of such disturbances. It is therefore suggested that baroclinic wave packets may be an important mechanism for forcing higher-frequency wave-2 disturbances observed in the real Southern Hemisphere stratosphere. The low-frequency stratospheric disturbances obtained in the nonlinear simulations appear to be associated with more subtle aspects of the baroclinic wave packets such as their spatial and temporal variability.

1. Introduction

There is strong evidence that much of the planetary wave activity observed in the wintertime stratosphere is excited in the troposphere (e.g., Randel 1987 and references therein). The most obvious tropospheric sources of planetary waves are associated with geographical asymmetries such as topography and spatially inhomogeneous heating (primarily due to land–sea contrasts). Stationary planetary wave patterns in the wintertime stratosphere are primarily due to these geographical asymmetries. Differences in the amplitudes of the geographical asymmetries between the Northern Hemisphere (NH) and Southern Hemisphere (SH) are reflected in corresponding interhemispheric differences in the planetary wave response in the wintertime stratosphere (e.g., Leovy and Webster 1976 and references therein). In the NH, where geographical asymmetries are large, the wintertime stratosphere is dominated by stationary planetary wave patterns. In the SH, where geographic asymmetries are relatively weak, a greater proportion of the planetary wave activity in the wintertime stratosphere is associated with travelling, rather than station-

* Current affiliation: Canadian Centre for Climate Modelling and Analysis, Atmospheric Environment Service, University of Victoria, Victoria, British Columbia, Canada.

+ The Centre for Atmospheric Science is a joint initiative of the Department of Applied Mathematics and Theoretical Physics and the Department of Chemistry, University of Cambridge, Cambridge, United Kingdom.

Corresponding author address: Dr. Peter H. Haynes, Centre for Atmospheric Science, Dept. of Applied Mathematics and Theoretical Physics, Silver Street, Cambridge CB3 9EW United Kingdom.
E-mail: phh@amtp.cam.ac.uk

ary, disturbances (e.g., Randel 1987; Manney et al. 1991; Yamazaki and Mechoso 1985; Mechoso et al. 1988).

Another important tropospheric source of planetary wave forcing is likely to be associated with synoptic-scale weather systems. Only the largest scale disturbances can propagate upward into the stratosphere. While the weather systems themselves have a spatial scale that is too small for effective upward propagation, the large-scale spatial organization of such systems can allow appreciable nonlinear forcing of long waves (Gall et al. 1979a,b; MacVean 1985; Young and Villere 1985; Young 1986). Such nonlinear forcing may well contribute to the week-to-week variability of the stratospheric circulation and help trigger major wave events such as sudden warmings. While it is clear that this type of nonlinear wave forcing is present in both the NH and SH winter tropospheres, its role is likely to be particularly important in the SH, where direct planetary wave forcing by geographical asymmetries is likely to be relatively weak.

At present the precise relation between stratospheric planetary amplitudes and the tropospheric circulation is not well understood. Some large-amplitude stratospheric wave events seem to be associated with particular disturbances to the tropospheric circulation. Others have no clear link to any particular aspect of the tropospheric circulation. In addition, there are occasions when the tropospheric circulation is highly disturbed but stratospheric waves remain weak (e.g., Randel et al. 1987; Manney et al. 1991).

The central aim of this paper is to investigate the tropospheric nonlinear longwave forcing mechanism and to understand the sort of variability it can induce in the wintertime stratospheric circulation. Our approach is to use idealized nonlinear numerical simulations employing a simple sigma-coordinate general circulation model based on that by Hoskins and Simmons (1975). The simulations are performed in a deep model domain in a forced–dissipative regime in which the tropospheric and stratospheric circulations are thermally relaxed toward zonally symmetric notional wintertime conditions. In this way baroclinic eddies are continually forced in the troposphere. The model does not include topography or any zonally asymmetric diabatic heating. Therefore, in these experiments, all longwave variability in the stratosphere is a direct consequence of nonlinear forcing associated with tropospheric baroclinic eddies. There is no externally imposed forcing on longwave scales.

Previous studies have considered various aspects of this problem. Numerical simulations have been used to investigate the longwave forcing mechanism and its response within the troposphere for both initial value simulations (Gall et al. 1979a,b; MacVean 1985; Young and Villere 1985; Young 1986) and forced–dissipative simulations (Hendon and Hartmann 1985; Hayashi and Golder 1987). Previous study of the stratospheric response to nonlinear tropospheric longwave forcing has been limited to initial-value problems (Young and Houben 1989; Duffy 1995). While these studies provide insight into the nonlinear longwave forcing mechanism and its impulsive response in the stratosphere, they do not throw any light on the question of the temporal variability of the stratospheric response.

In the present study, long integrations show the continual growth and decay of baroclinic eddies in the troposphere, with intermittent events in which there is significant propagation of long waves, sometimes wavenumber 1, sometimes wavenumber 2, up into the stratosphere. The planetary wave amplitudes in these experiments are approximately half the value of those typically observed in the SH wintertime stratosphere. However, there are striking similarities between the form of the observed variability in the SH winter stratosphere and the form of the stratospheric variability produced in the very simple experiments performed here. The important point is that longwave variability in the stratosphere can arise purely through the internal variability of the tropospheric baroclinic eddies.

In order to gain further insight into those aspects of the tropospheric flow that are important to the forcing of stratospheric long waves, we carry out the following analysis. The prognostic variables of the governing equations are separated into a zonal average plus deviation and the model equations are then Fourier decomposed in the zonal direction. If the nonlinear terms are considered as externally imposed forcing, and the zonal-mean basic state is specified, then this procedure results in a linear system of equations for each zonal wavenumber. The time history of nonlinear eddy forcing terms and the zonal-mean basic state are determined from the full nonlinear simulation. These are then used to integrate the linear system forward in time, in the absence of the baroclinic eddies, for each planetary-scale zonal wavenumber. The desired result is a full reconstruction of the stratospheric response by the forced linear model.

The ability to reconstruct the response with the forced linear model allows us to investigate the causal connection between the nonlinear longwave forcing and the stratospheric response in the full nonlinear system. Nonlinear eddy forcing terms appear in the vorticity, divergence, temperature, and surface pressure equations. In a series of forced linear model experiments, different spatial and temporal filters are applied to the forcing and the differences in the response are analyzed. These show that (i) that both eddy vorticity forcing and eddy temperature forcing are required to account for the planetary wave response, but that the effects of both eddy divergence and eddy surface pressure forcing is negligible; (ii) only the eddy vorticity forcing and eddy temperature forcing of the long waves are required to reproduce the stratospheric planetary wave response; (iii) only the low-frequency component of the nonlinear tropospheric forcing is important; (iv) the vertical structure of the forcing displays maxima near tropopause level;

and (v) in the experiments, the variability of the planetary wave response in the stratosphere arises primarily from the variability of the nonlinear eddy forcing in the troposphere, rather than from the variability of the wave propagation characteristics associated with the basic-state zonally averaged flow.

This latter conclusion distinguishes the mechanism for stratospheric planetary wave variability that occurs in the numerical simulations reported here from that previously suggested by Chen and Robinson (1992). Chen and Robinson have suggested that variability of the basic-state static stability and vertical wind shear at the tropopause could act as a ''valve'' for upward-propagating planetary waves, providing a source of planetary wave transience in the stratosphere. The absence of this mechanism in the numerical simulations reported here is due to the fact that the zonally averaged flow displays only weak variability.

The requirement of both the eddy vorticity and eddy temperature forcing fields, for the adequate reconstruction of the stratospheric planetary wave response in the forced linear model, makes it difficult to characterize the structure of the nonlinear wave forcing (i.e., there may be significant cancellation between the two eddy forcing fields). This parallels the situation encountered for the the Eulerian zonal-mean equations (e.g., Andrews et al. 1987, section 3.5). Following this example, we undertake a transformation of the forced linear system designed to combine all of the eddy forcing into a single term in one of the prognostic equations. This is done in analogy with the transformed Eulerian mean (TEM) formalism. We shall refer to this procedure as the transformed Fourier decomposition (TFD).

A forced linear model employing the TFD equations is then used for several experiments in which we simplify the vertical structure of the nonlinear wave forcing. The analysis indicates that the vertical structure of the eddy forcing is equivalent to a compact source near tropopause level. In addition, the TFD transformation provides a single representation of the nonlinear wave forcing and we analyze its spatial and temporal characteristics.

The outline of the paper is as follows. In section 2 we describe the numerical model and the details of the numerical simulations. In section 3 we analyze the response of the numerical simulation in both the stratosphere and troposphere, and compare the response with observations from the Southern Hemisphere. In section 4 we employ the forced linear model to gain insight into the nature of the eddy forcing of planetary waves in the troposphere. In section 5 we derive the transformed Fourier decomposition and use it to simplify to the relevant eddy forcing down to one scalar field. In section 6 we apply simple linear wave theory to additional forced linear model experiments in an attempt to understand the differences between the numerical simulations and observations that were identified in section 3. Finally, in section 7 we conclude with a brief discussion the results of the present study.

2. Numerical model and experimental parameters

The experiments described in this paper employ the sigma-coordinate spectral model developed by Hoskins and Simmons (1975). The experiments are conducted in a hemispheric domain (i.e., with rigid boundary at the equator) and, unless otherwise stated, the truncation of the spectral horizontal resolution is triangular at total wavenumber 42 (T42). The model domain employs 30 vertical levels. The vertical spacing of the model levels is linear with respect to σ in the troposphere and logarithmic with respect to σ in the stratosphere and above. The elevations of the model levels are specified in the appendix.

The model integrations employ ∇^6 diffusion applied to the vorticity, divergence, and temperature equations with a decay rate of 6 d^{-1} for the smallest scale, $n = 42$. Surface drag in the form of Rayleigh friction is applied in the lowest model level with a timescale of 0.5 days. A deep absorbing layer in the uppermost 12 levels of the model is also employed to prevent spurious reflections from the model lid.

The initial flow is zonally symmetric and represents notional winter climatology. The initial zonal wind field is displayed in Fig. 1. It is composed of a tropospheric jet at 30° latitude with a peak wind speed of 40 m s^{-1} and a stratospheric–mesospheric jet at 50° latitude with a peak wind speed of 60 m s^{-1}. The functional form of the initial zonal wind is given in the appendix. The initial temperature field, also displayed in Fig. 1, is specified as the *U.S. Standard Atmosphere 1976* vertical profile (e.g., Fels 1986) with a meridional structure that is in thermal wind balance with the initial zonal wind field (e.g., Hoskins and Simmons 1975).

Baroclinic instability is initiated in the model by the application of white-noise perturbations to the surface pressure field at $t = 0$. In a series of forced–dissipative experiments the baroclinicity of the basic state is maintained by the application of Newtonian cooling with a 25-day timescale toward the initial zonally symmetric temperature distribution. As a consequence, there is no external forcing of planetary-scale disturbances during the entire flow evolution.

An additional T42 experiment was performed using ∇^8 diffusion with a decay rate of 8 d^{-1} on the smallest scale. The results of this simulation were found to remain essentially unchanged from the results of the ∇^6 simulation, which are presented below.

3. Nonlinear simulations

a. Impulsive development of long waves

Before considering the dynamics of the forced–dissipative system, it is first useful to consider the impul-

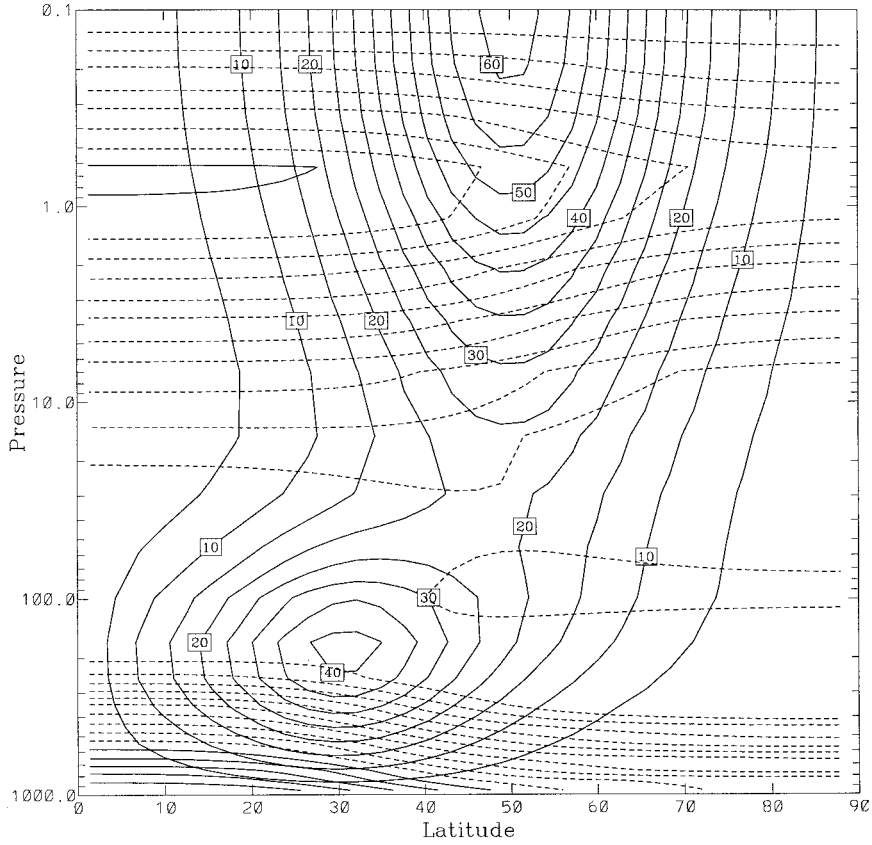

FIG. 1. Basic-state zonal wind and temperature fields employed for the numerical simulations. These were used as initial conditions for the initial value simulation and the the temperature was used as a reference state for the thermal relaxation in the forced–dissipative simulations. The contour intervals are 5 m s^{-1} for the wind and 10°C, with temperatures less than 0°C indicated by dashed lines.

sive development of the long waves from the synoptic-scale eddies. A 50-day initial value simulation was performed in which the 25-day Newtonian cooling was switched off. All other details of this simulation are identical to those described in section 2. In Fig. 2 the natural logarithm of domain-integrated kinetic energy (top panel) and the time rate of this quantity multiplied by one-half (lower panel) is displayed as a function of zonal wavenumber and time. For exponentially growing disturbances the quantity shown in the lower panel corresponds directly to the growth rate. Exponential growth of the synoptic-scale eddies (zonal wavenumbers 6–9) occurs from day 10 to day 25 of the initial-value simulation. A linear stability analysis of the initial flow was performed (e.g., Wyatt 1981) and calculated growth rates for the synoptic-scale wavenumbers compare to within 15% of those displayed in Fig. 2, during the period of days 10–25 when linear growth is relevant.

The important feature in Fig. 2 is the growth of long waves that occurs from day 20 to 30. The maximum growth of the long waves near day 25 is nearly twice the growth rate of the synoptic-scale waves. The dramatic growth of long waves in the troposphere obtained in such initial-value simulations was first investigated by Gall et al. (1979a, Fig. 2) and identified as due to nonlinear wave–wave interactions of the synoptic-scale eddies (Gall et al. 1979a,b; MacVean 1985; Young and Villere 1985; Young 1986). It is clear that longwave forcing in an equilibrated forced–dissipative problem must arise as a result of the same nonlinear wave–wave interaction of the synoptic-scale eddies. However, the equilibrated form and strength of such nonlinear wave forcing, and its longwave response in the troposphere and stratosphere, cannot be inferred from the evolution of the initial-value problem.

b. Stratospheric response in the forced–dissipative regime

A 1050-day forced–dissipative simulation was performed. In order to identify events in which planetary waves are forced and propagate up into the stratosphere we consider the evolution of upward Eliassen–Palm (E–P) flux. In Fig. 3 the time series of meridionally integrated upward E–P flux is displayed for zonal waves 1–4 (Figs. 3a–d) as a function of height. Intermittent bursts

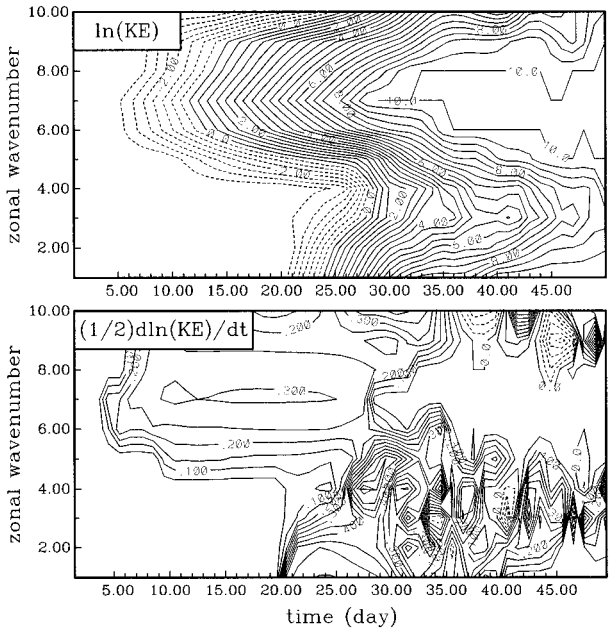

FIG. 2. The natural logarithm of domain integrated kinetic energy (top) and one-half its tendency (bottom) as a function of zonal wavenumber and model time from the initial value simulation. Contours in the bottom figure can be interpreted as the growth rate of exponentially growing disturbances. The contour interval in the bottom figure is 0.05 d^{-1}. The normal-mode exponential growth of the synoptic scales (waves 6–9) occurs from day 10 to 25. Due to wave–wave interactions of the synoptic-scale eddies, rapid growth of the long waves (1–3) occurs from day 20 to 30.

of upward-propagating wavenumber 1 and wavenumber 2 (hereafter wave-1 and wave-2) are apparent over the entire time series.

Local extrema of upward E–P flux in Fig. 3 indicate that upward-propagating wave events occur with a range of timescales upward from 10 days. For example, from days 200 to 500 wave-1 displays three groups of wave events centered on day 250, 350, and 450. Each group comprises approximately 4–5 events that are each separated by roughly 10 days. Over the same period, wave-2 events appear more sporadic with upward bursts separated by 10–50 days (see Fig. 5 for more detail).

The time histories of wave-1 and wave-2 geopotential height amplitudes on the 10-mb pressure level are displayed as a function of latitude in Figs. 4a and 4b (contour interval 100 m). Maximum wave amplitudes of 300–500 m and 200–400 m occur for wavenumbers 1 and 2, respectively, near latitudes corresponding, as expected (e.g., Simmons 1974), to the center of the stratospheric jet. A first comparison of the time series of wave-2 geopotential height (Fig. 4b) with observed Southern Hemisphere wave-2 amplitudes over 10 winters (Manney et al. 1991, Fig. 2) indicates similar patterns of meridional and temporal variation. The amplitude of wave-2 events, however, are approximately a factor of 2 smaller in the numerical simulation.

Frequency spectra of wave-1 and wave-2 geopotential height fluctuations at 10 mb, as a function of latitude, are respectively displayed in Figs. 4c and 4d. Positive frequency corresponds to eastward phase propagation. Both wave-1 and wave-2 disturbances at 10 mb display only low-frequency structure with little power in periods less than 15 days. Wave-1 displays predominant westward phase propagation while wave-2 is predominantly eastward with some westward phase propagation. The frequency spectra in Figs. 4c and 4d were derived from time series spanning the entire simulation. Details of the frequency spectra appear to be sensitive to truncating the full time series. However, the low-frequency nature of the wave-1 and wave-2 response at 10 mb appears to be robust.

The observational study by Manney et al. (1991) of wave-2 in the SH wintertime stratosphere indicated both ''fast'' (5–12 d period) and ''slow'' (20–30 d period) transients, which were always eastward propagating. The fast transience of wave-2 appears to be absent in the idealized numerical simulation considered here. Also, wave-2 in the numerical simulation has both eastward and westward phase propagation at 10 mb.

The appearance of westward-propagating wave-2 in the numerical simulation, but not in the observations, and the absence of rapidly eastward-propagating disturbances in the numerical simulation may be explained by the strength of the stratospheric winds. The observed time-mean zonal-mean zonal wind in the lower stratosphere SH winter (e.g., see Randel 1992) is much stronger than the equilibrated winds in the numerical simulation (e.g., see Fig. 18a later). The Charney–Drazin theorem (e.g., Andrews et al. 1987) suggests that the range of phase speeds that corresponds to upward propagation shifts toward positive (eastward) phase speeds as the basic-state westerly wind is strengthened. This is confirmed later in section 6a by explicit application of a linear model analysis. As a consequence, westward-propagating wave-2 disturbances should be more strongly filtered by the observed winds and fast eastward-propagating wave-2 disturbances should be more strongly filtered by the weaker winds that develop in the numerical simulation.

A detailed time history of wave-2 events is displayed in Fig. 5 from day 200 to 500. Figure 5a displays the wave-2 geopotential height amplitude on the 10-mb pressure level as a function of latitude, Fig. 5b displays wave-2 geopotential height amplitude at 60° latitude as a function of height, and Fig. 5c displays the wave-2 meridionally integrated upward E–P flux as a function of height. Almost all of the events on the 10-mb surface (Fig. 5a) can be identified with bursts of upward E–P flux (Fig. 5c). Many of the events at 10 mb can be traced back into the troposphere following contours of geopotential height amplitude (Fig. 5b). The upward E–P flux might be expected to be a better indicator of stratospheric wave events that originate in the troposphere. However, there are wave events that are difficult to trace back into the troposphere, even using the upward E–P

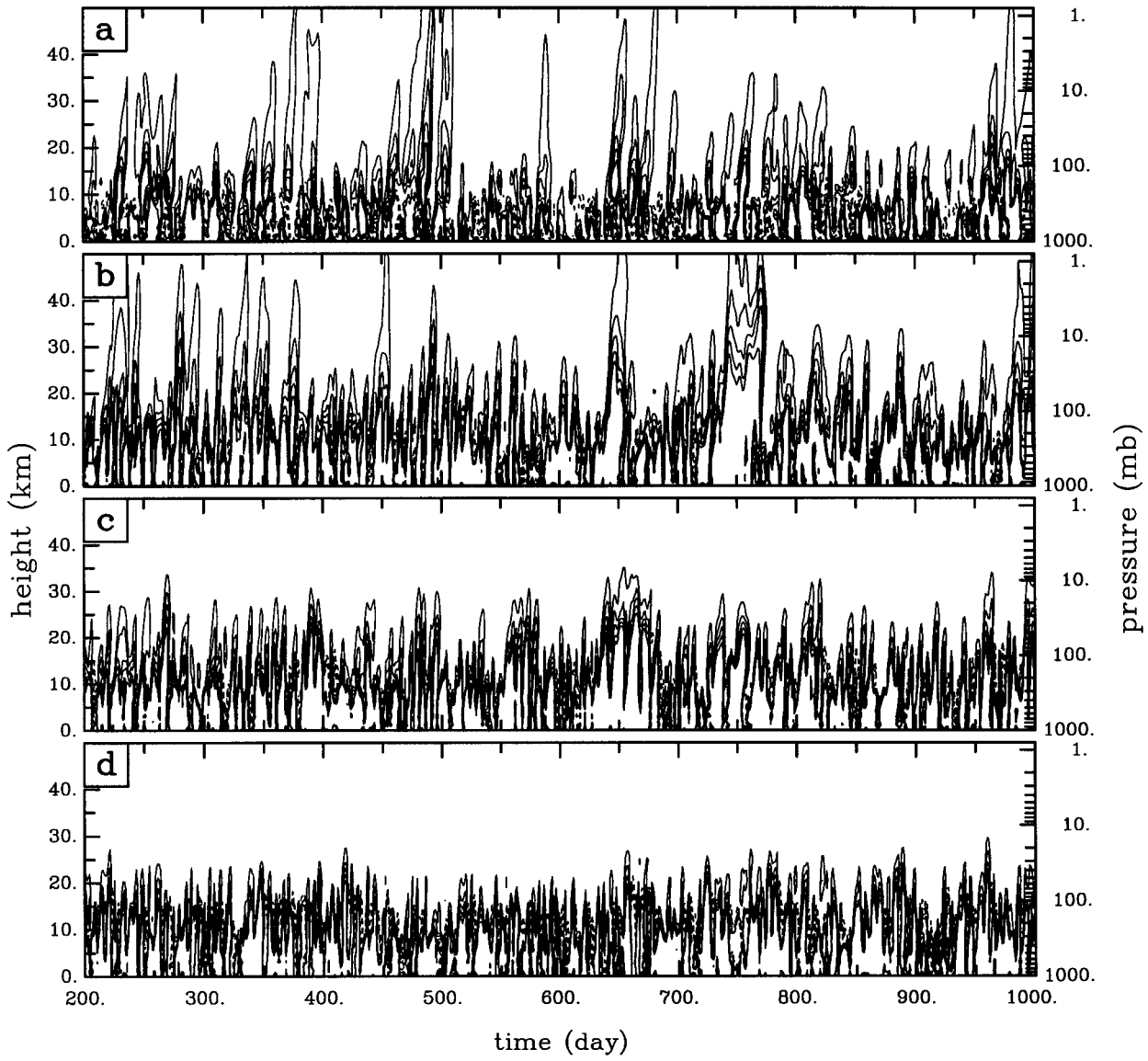

FIG. 3. Time–height plots of latitudinally integrated upward E–P flux from the forced–dissipative simulation. Waves 1–4 are, respectively, displayed in (a)–(d). The contour interval is 1.7×10^{17} m^3 Pa.

flux signal. For example, a very fine contour interval in the the upward E–P flux (Fig. 5c) is required to indicate that the two adjacent events that occur near day 397 and 414 (in Fig. 5a) have a link back to the troposphere.

Similar events in the SH wintertime stratosphere, with tenuous tropospheric links, have been identified by Manney et al. (1991), who suggest in situ instability of the stratospheric flow as a possible explanation. However the forced linear model experiments, discussed later in section 7, support the conclusion that such events arising in the numerical simulation are not associated with instability.

In order to quantify the upward propagation of each planetary wave in the numerical simulation, we consider time-lag cross-correlation analyses of the geopotential height field (e.g., Randel 1987, section 2). Figure 6 displays the correlation of the time series of geopotential height fluctuations at 10 mb and 52° latitude (indicated by X in Fig. 6) with time series of geopotential height fluctuations at 52° and all other elevations as a function of time lag for planetary waves 1–4 (Figs. 6a–d, respectively). Each planetary wave displays a strong correlation between the stratosphere and upper troposphere. Below 10 mb, the maximum correlation for waves 1–3 tilts backward in time, suggesting the troposphere as the source of planetary wave disturbances.

In Fig. 6, wave-1 and wave-2 display respective time lags of approximately 7 and 5 days for the propagation time between the upper troposphere and 10 mb. Time-

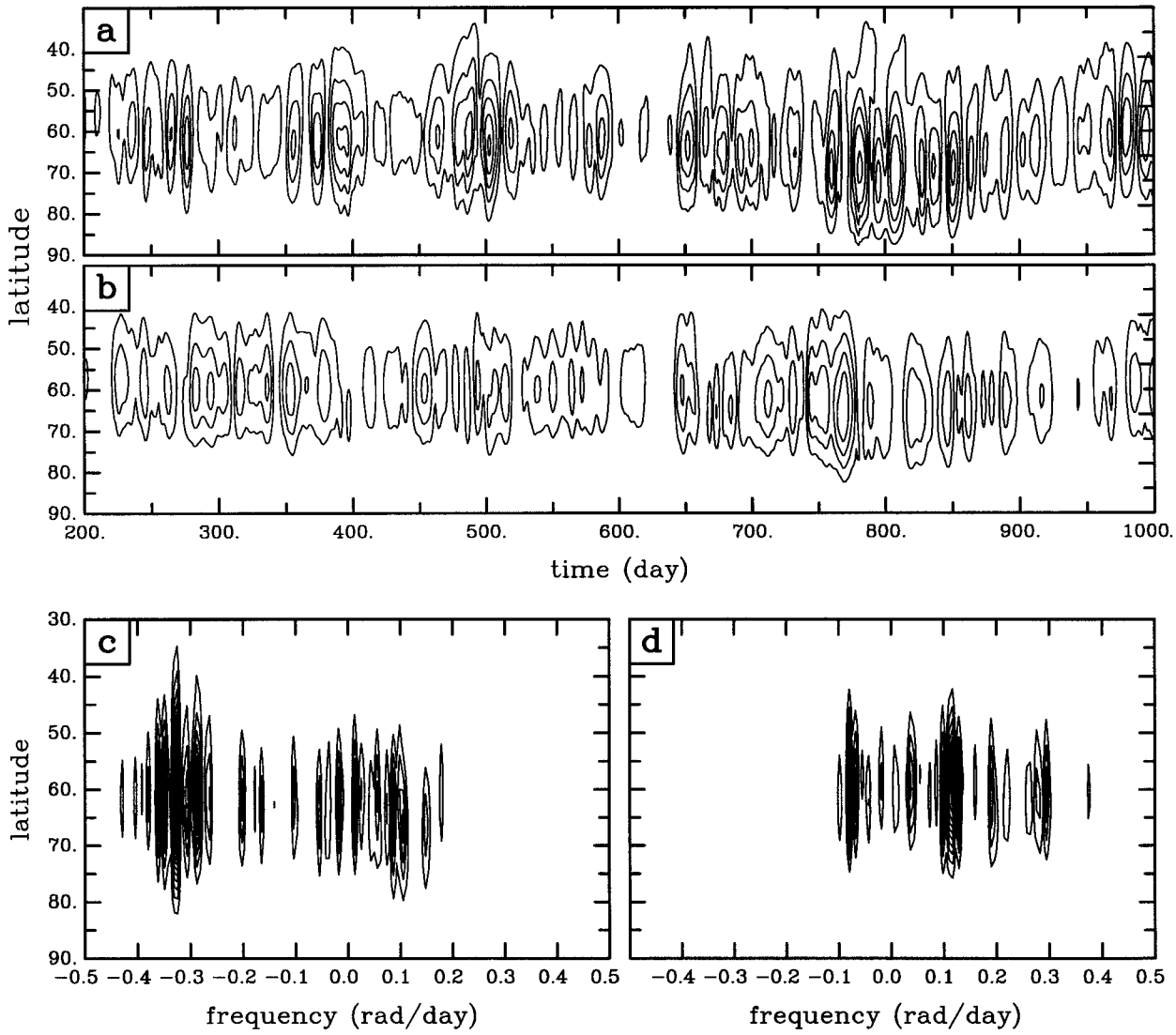

FIG. 4. (a), (b) Time–latitude plots of geopotential height amplitudes on the 10-mb pressure surface for waves 1 and 2, respectively. The contour interval is 100 m. (c), (d) Frequency–latitude power spectra of geopotential height amplitudes on the 10-mb pressure surface for waves-1 and 2, respectively.

lag correlations of SH wintertime geopotential height fluctuations calculated by Randel (1987) also indicate the tendency toward shorter propagation time for larger planetary-scale wavenumbers, but the propagation speed of each planetary wavenumber is almost twice that seen in the numerical simulation.

In Fig. 6, wave-3 also displays upward propagation and has a time lag of roughly 2 days from the upper troposphere to 10 mb. The time-lag correlations for wave-4 display very little tilt with height, indicating the well-known tendency for planetary waves to become evanescent with height with increasing zonal wavenumber. The maximum geopotential height amplitudes of wave-3 and wave-4 at 10 mb (not shown) are 100 and 50 m, respectively. This would indicate that the transition from propagating to evanescent disturbances occurs near wave-4.

In section 6 we use linear theory to consider the functional dependence of vertical group velocity on the zonal wavenumber and intrinsic frequency. This provides a qualitative understanding of the upward propagation characteristics of the planetary waves displayed in Fig. 6 and an understanding of why their upward group speeds differ from observations.

c. Tropospheric circulation in forced–dissipative regime

In the forced–dissipative simulation the baroclinic eddies in the troposphere persistently organized them-

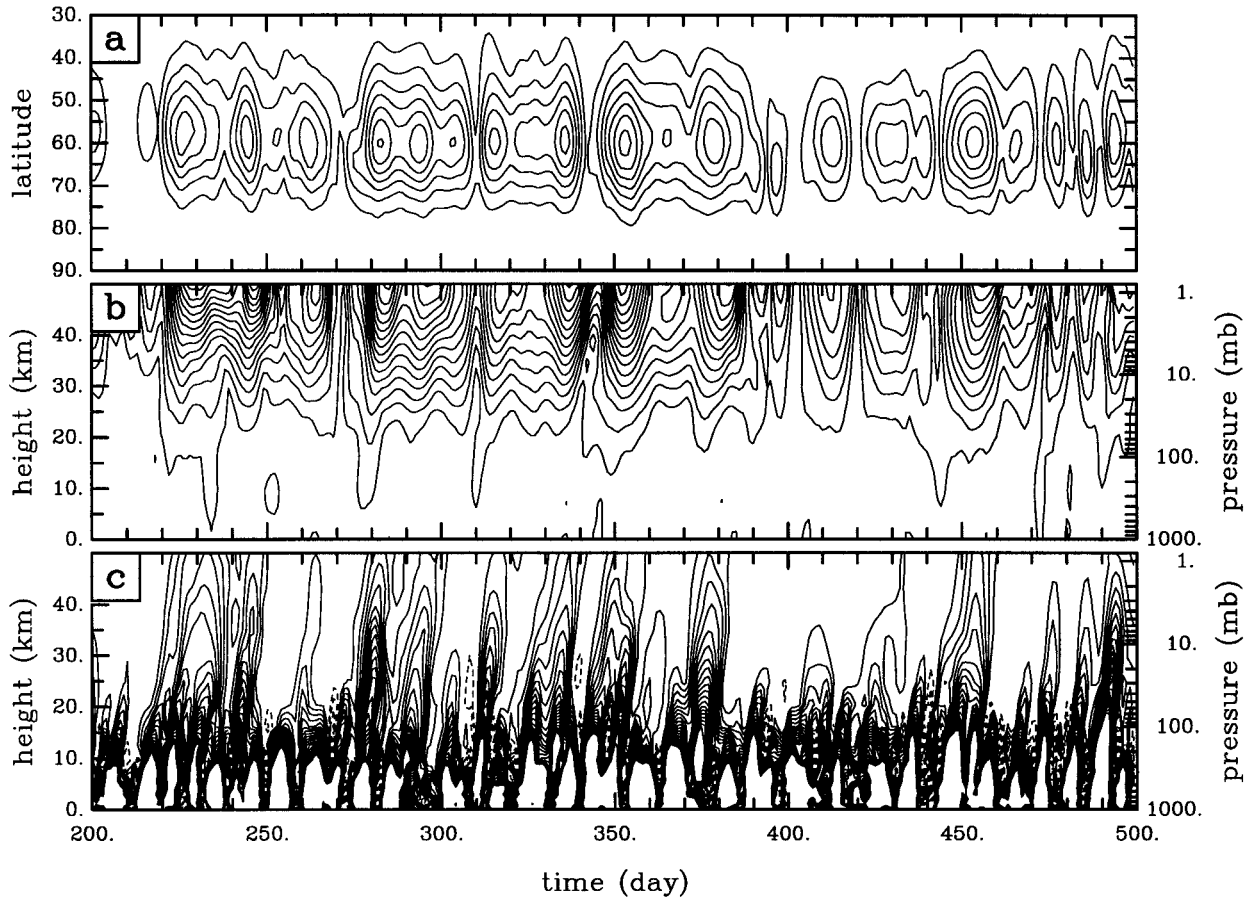

FIG. 5. (a) Wave-2 time–latitude plots of geopotential height amplitudes on the 10-mb pressure surface (contour interval 50 m), (b) wave-2 time–height plots of geopotential height amplitude at 60° latitude (contour interval 50 m), (c) wave-2 time–height plots of latitudinally integrated upward E–P flux (contour interval is one-third of that used in Fig. 3).

selves into packet structures. A Hovmöller plot of the northward component of velocity at 45° latitude on the 350-mb pressure surface is displayed in Fig. 7 as a function of longitude. It is immediately apparent from Fig. 7 that the eddies are highly organized. There appear to be two propagation velocities associated with the eddies. One is the phase speed of the eddies, which ranges from 3 to 7 m s^{-1}. The second is the group velocity of the packets of eddies, which is much faster and ranges from 21 to 28 m s^{-1}. The packets exhibit extended periods of relatively regular (e.g., days 150–225) and irregular (e.g., days 275–325) behavior.

The tendency of the baroclinic eddies to organize themselves into packet structures is not believed to be a consequence of the idealizations employed in the numerical simulation. Observations of transient baroclinic eddies in the SH troposphere indicate a similar tendency toward packet structures (Lee and Held 1993; Berbery and Vera 1996). The tropospheric circulation in the present simulations is not unrealistic in this sense.

In the present numerical simulation the dominant envelope structure of the packets is almost exclusively wave-2. This can be seen in Fig. 8 where we present polar stereographic plots of northward component of velocity on the 350-mb pressure surface for days 201–206. This period of time roughly corresponds to the time it takes the wave-2 packet structure to propagate halfway around a latitude circle (i.e., the period of the wave-2 packet). This rapid sequence also illustrates the relation between the evolution of the eddies and the evolution of the packet structures. It is clear from Fig. 8 that both are eastward propagating. Over the whole sequence, as each packet propagates around 180°, the development of the individual eddies within the packets can be identified. As an example, the eddy centered on 280° longitude (where 0° longitude corresponds to the very bottom of the projection) on day 201 amplifies as it moves through the leading edge of the packet (day 201–203) and decays as it moves through the trailing edge of the packet day (204–206). This evolution has been previously identified and discussed in numerical simulations conducted by Lee and Held (1993) (see also Esler 1997).

The presence of envelope structures of the baroclinic eddies indicates that there is a range of synoptic-scale wavenumbers present in the flow (centered on the dominant wavenumber within the packet and with spectral

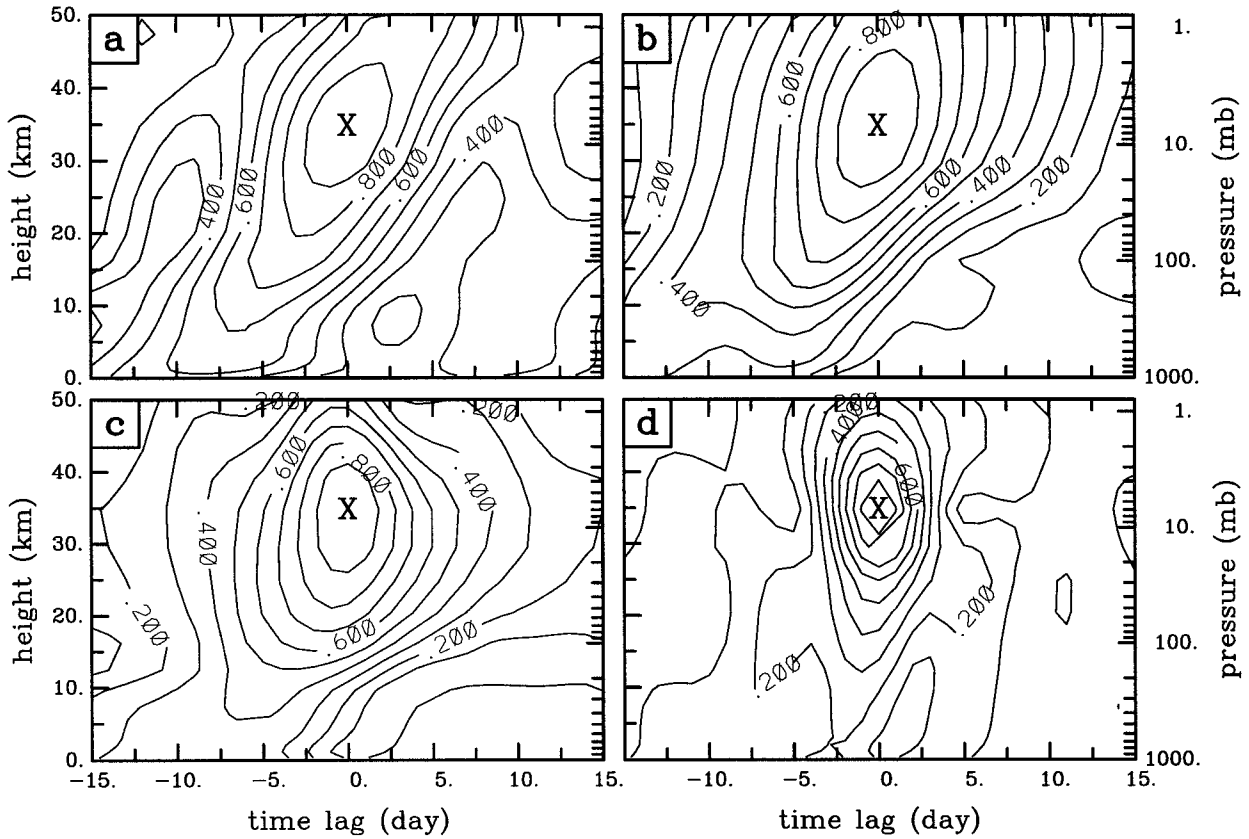

FIG. 6. Correlation coefficient of the time series of geopotential height fluctuations at 10 mb and 52° latitude (indicated by X) with time series of geopotential height fluctuations at 52° latitude and all other elevations as a function of time lag for planetary waves 1–4 (panels a–d, respectively).

width corresponding to the wavenumber of the envelope structure). Nonlinear interaction between the different synoptic-scale wavenumbers gives the possibility of nonlinear forcing at wavenumbers close to the envelope wavenumber. From an alternative viewpoint, the nonlinear terms are largest within each packet, have a nonzero average over each packet, and hence will tend to force at the wavenumber of the packet (i.e., the envelope scale).

It is almost certain that the dominant wave-2 structure of the baroclinic wave packets corresponds to a strong wave-2 forcing in the troposphere (this is verified in section 4c; see, e.g., Fig. 14c). If the timescale associated with the most intense wave-2 forcing takes on values typical of the periods associated with the packets, this would imply strong wave-2 forcing with periods of 5–8 days. However, it is clear from Fig. 4d that at these short periods there is no significant wave-2 response at 10 mb. This raises the question of the precise connection between the packet organization of the baroclinic eddies in the troposphere and the planetary-wave transience illustrated in Fig. 4.

The absence of such rapid wave-2 transience in the stratosphere appears to be due to the filtering of such disturbances by the basic-state winds (i.e., the basic-state flow does not support upward-propagating disturbances at this spatial scale and temporal frequency). Wave-2 periods of 5–8 days correspond to phase speeds of approximately 25 m s^{-1} at midlatitudes. A simple application of the Charney–Drazin theorem would predict upward propagation if the weakest winds in the jet core were greater than 25 m s^{-1}. The time-mean zonal-mean zonal winds of the numerical simulation (Fig. 18a), indicate that the weakest winds in the jet core (near 40 mb) are about 25 m s^{-1} and, therefore, on the threshold of this criterion. To determine whether the upward propagation of wave-2 disturbances at such high frequencies is inhibited therefore requires a more thorough investigation. This is carried out in section 6c, where we consider how strong the zonal wind in the jet core must be in order for such high-frequency transience to impact significantly the stratospheric response.

It is clear that, in the numerical simulation, one cannot directly relate the lower-frequency planetary wave transience in the stratosphere with the dominant characteristics of the baroclinic wave packets in the troposphere. If the two are related it would seem to be in a more subtle manner. For example, it may be variability of the packet structures is the most important property relevant

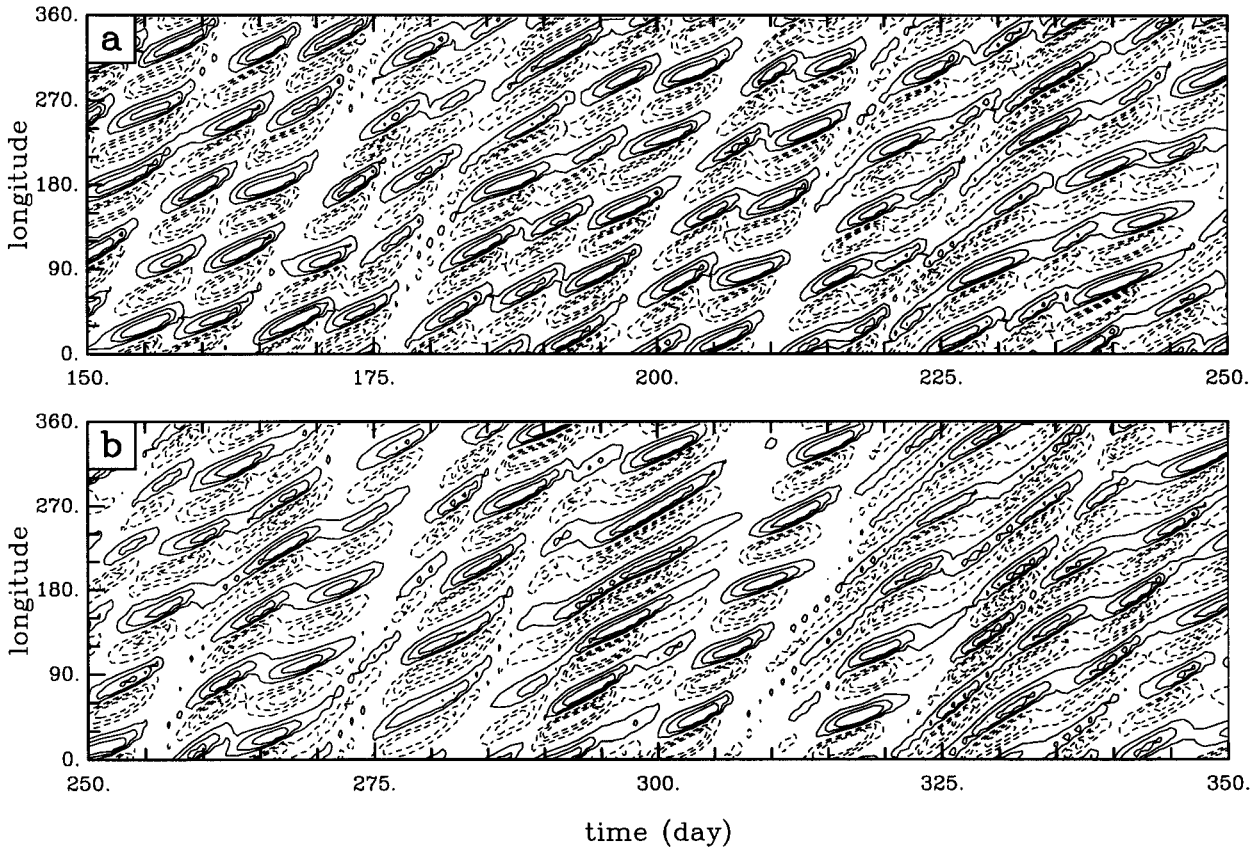

FIG. 7. Time–longitude plot of the northward component of velocity at 45° latitude on the 350-mb pressure surface. The contour interval is 10 m s^{-1}. (a) 150–250 days. (b) 250–350 days.

to the forcing of low-frequency planetary-scale disturbances in the troposphere.

It is important to point out that the planetary-scale envelope structures in Fig. 8 do not directly represent a forcing of planetary scales (e.g., a zonal Fourier decomposition of the northward component of velocity in Fig. 8 would only reveal significant power in the synoptic-scale wavenumbers). In order to investigate the forcing, one must identify the relevant nonlinear terms in the governing equations and identify their net contribution to planetary scales. In order to investigate the stratospheric response, one would then have to determine how this nonlinear forcing projects onto planetary-scale disturbances that can propagate up into the stratosphere. In the next section, we develop diagnostics that allow us to address these issues.

4. Forced linear model experiments

In this section we derive a diagnostic tool, the forced linear model, used to investigate the nature of the nonlinear eddy-forcing mechanism and its relation to the stratospheric planetary wave variability identified in the nonlinear simulations. We begin by defining the forced linear model. Next, we outline the procedure by which the forced linear model is used to analyze the nonlinear simulations. Finally, we describe a series of forced linear model experiments, which are summarized in Table 1.

a. Definition of forced linear model

The sigma-coordinate primitive equations may be written schematically as

$$\frac{\partial \mathbf{x}}{\partial t} + \mathcal{L}(\mathbf{x}) + \mathcal{N}(\mathbf{x}) = \mathcal{D}(\mathbf{x}), \tag{1}$$

where $\mathbf{x}$ is a vector representing the prognostic variables (i.e., the horizontal velocity $\mathbf{u}$, the temperature T, and the surface pressure p_*), $\mathcal{L}(\,)$ is an operator that is linear in the prognostic variables, $\mathcal{N}(\,)$ is a nonlinear operator that is quadratic in the prognostic variables (representing terms such as $\mathbf{u}\cdot\nabla T$) and $\mathcal{D}(\,)$ represents frictional and diabatic processes, which are assumed linear in the prognostic variables.

Letting $\mathbf{x} = \overline{\mathbf{x}} + \mathbf{x}'$ in (1), where $\overline{\mathbf{x}}$ represents a zonal average, we first note that $\mathcal{N}(\overline{\mathbf{x}} + \mathbf{x}') = \mathcal{N}(\overline{\mathbf{x}}) + \mathcal{N}(\mathbf{x}') + \mathcal{L}_N(\overline{\mathbf{x}}, \mathbf{x}')$, where $\mathcal{L}_N(\overline{\mathbf{x}}, \mathbf{x}')$ is linear in each of $\overline{\mathbf{x}}$ and $\mathbf{x}'$. We may then write a set of equations that governs the deviations $\mathbf{x}'$ away from the the zonal mean $\overline{\mathbf{x}}$:

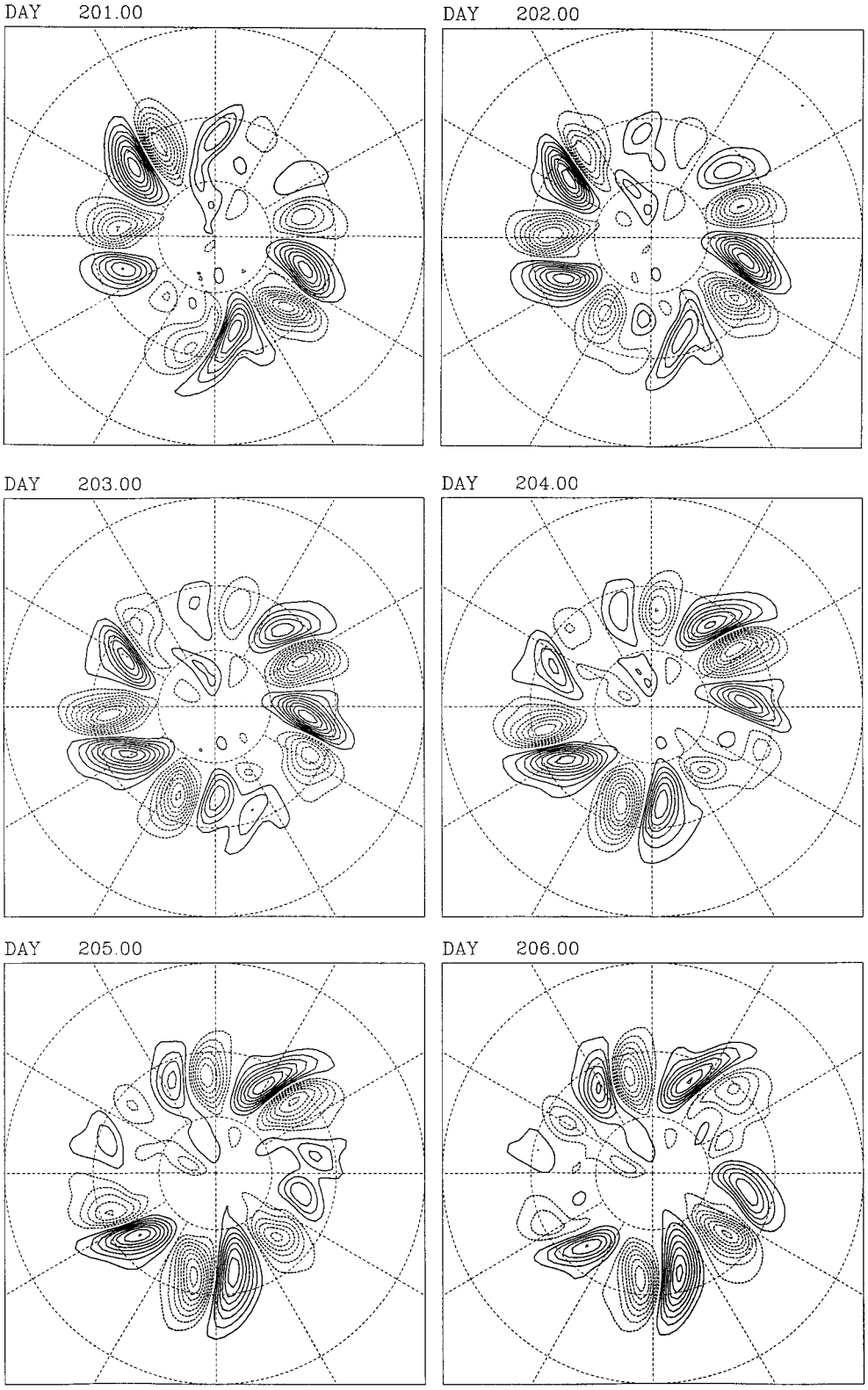

FIG. 8. Polar stereographic plots of northward component of velocity on the 350-mb pressure surface from day 201 to 206, roughly corresponding to one period of the wave-2 packet propagation. The contour interval is 5 m s^{-1}.

TABLE 1. Correlations for forced linear–model experiments.

Exp.	Forcing elevation	Fields forced F_k	Basic state U	Corr run	Mean Φ Correlation [30°, 70°], $k = 1$	Mean Φ Correlation [20 km, 40 km] $k = 2$
F1	≤50 km	all	time evolving	A0	0.981	0.986
F2	≤50 km	all	time mean [100 d, 400 d]	A0	0.846	0.748
F3	≤20 km	all	time evolving	A0	0.850	0.853
F4	≤20 km	F_k^ζ, F_k^T	time evolving	F3	0.975	0.974
				A0	0.821	0.828
F5	≤20 km	F_k^ζ	time evolving	F4	0.773	0.549
				F3	0.734	0.501
F6	≤20 km	F_k^T	time evolving	F4	0.259	0.546
				F3	0.284	0.567
F7	≤20 km	$F_k^T \times (1 - e^{[-(z/4)^2]})$	time evolving	F6	0.935	0.926
Vertical structure: vertically integrated [0, 20] km, imposed form: $\propto \sin^2[\pi(z - z_1)/(z_2 - z_1)]$, $z_1 \le z \le z_2$						
V1	z_1, z_2 = 2.5, 17.5 km	F_k^ζ	time evolving	F5	0.880	0.798
V2	z_1, z_2 = 5, 15 km	F_k^ζ	time evolving	F5	0.857	0.801
V3	z_1, z_2 = 2.5, 17.5 km	F_k^T	time evolving	F6	0.513	0.689
Meridional structure: meridional average (a)/window (w), imposed form/window: $\propto e^{[(\phi - \phi_1)/(\phi_2)]^2}$						
	≤20 km					
M1	(a) ϕ_1, ϕ_2 = 45°, 15°	F_k^ζ, F_k^T	time evolving	*F*4	0.176	0.217
M2	(w) ϕ_1, ϕ_2 = 45°, 15°	F_k^ζ, F_k^T	time evolving	*F*4	0.517	0.670
M3	(w) ϕ_1, ϕ_2 = 45°, 25°	F_k^ζ, F_k^T	time evolving	*F*4	0.773	0.882
Temporal structure: Low-pass frequency filter, cutoff frequency $2\pi/P$						
	≤20 km					
T1	P = 20 d	F_k^ζ, F_k^T	time evolving	*F*4	0.870	0.862
T2	P = 15 d	F_k^ζ, F_k^T	time evolving	*F*4	0.932	0.913
Transformed Fourier decomposition:						
TFD1	≤20 km	$F_k^{\zeta+T}$	time evolving	F4	0.879	0.726
				F3	0.827	0.647
TFD2	vertically integrated z_1, z_2 = 5, 15 km	$F_k^{\zeta+T}$	time evolving	TFD1	0.830	0.760
				F4	0.784	0.644
				F3	0.750	0.600

$$\frac{\partial \mathbf{x}'}{\partial t} + \mathcal{L}(\mathbf{x}') + \mathcal{L}_N(\overline{\mathbf{x}}, \mathbf{x}') - \mathcal{D}(\mathbf{x}') = -[\mathcal{N}(\mathbf{x}') - \overline{\mathcal{N}(\mathbf{x}')}], \tag{2}$$

where all the terms on the left-hand side are linear in $\mathbf{x}'$.

The original system of equations (1) can be expressed as

$$\frac{\partial \overline{\mathbf{x}}}{\partial t} + \mathcal{L}(\overline{\mathbf{x}}) + \mathcal{N}(\overline{\mathbf{x}}) - \mathcal{D}(\overline{\mathbf{x}}) = -\overline{\mathcal{N}(\mathbf{x}')}, \tag{3}$$

$$\frac{\partial \mathbf{x}_k'}{\partial t} + \mathcal{L}(\mathbf{x}_k') + \mathcal{L}_N(\overline{\mathbf{x}}, \mathbf{x}_k') - \mathcal{D}(\mathbf{x}_k') = -\mathcal{N}(\mathbf{x}')_k, \tag{4}$$

that is, one set of equations (3) that govern the evolution of the zonal-mean flow $\overline{\mathbf{x}}$, and one set of equations (4) for each longitudinal wavenumber k ($\neq 0$) that govern the evolution of disturbance amplitudes $\mathbf{x}_k'$. The set of equations (4) is obtained by Fourier decomposing (2) in the zonal direction. In both (3) and (4) the nonlinear eddy-forcing terms have been taken to the right-hand side. The term $\overline{\mathcal{N}(\mathbf{x}')}$ represents nonlinear eddy forcing of the zonal-mean flow, while the term $\mathcal{N}(\mathbf{x}')_k$ represents nonlinear eddy forcing of the amplitude of wavenumber k.

In the present study the ''forced linear model'' is defined as

$$\frac{\partial \mathbf{x}_k'}{\partial t} + \mathcal{L}(\mathbf{x}_k') + \mathcal{L}_N(\mathbf{X}, \mathbf{x}_k') - \mathcal{D}(\mathbf{x}_k') = -\mathbf{F}_k, \tag{5}$$

where $\mathbf{X}$ is a vector representing a prescribed (generally time evolving) zonal-mean basic state, $\mathbf{F}_k$ is a vector of prescribed forcing for each zonal wavenumber k, and all other notation is as defined above. The systems (3) and (4) are formally identical to (5) if we take $\mathbf{X} = \overline{\mathbf{x}}$ and $\mathbf{F}_k = \mathcal{N}(\mathbf{x}')_k$. The model defined by (5) is linear in the sense that, given $\mathbf{X}$ and $\mathbf{F}_k$, each wavenumber may be integrated independently. In practice, we will be concerned with the response of the forced linear model for planetary-scale waves-1 and 2 only.

Of course, the decomposition leading to (5) is a purely formal one, in the sense that it may sometimes not make sense to impose the forcing term $\mathbf{F}_k$ as given. For ex-

ample, it might be that that effect of the nonlinear terms in the equation for wavenumber k is systematically to dissipate that wavenumber, in which case it might make more sense to reexpress $\mathbf{F}_k$ as, for example, $\mathcal{D}_N(\mathbf{x}, \mathbf{x}'_k)$ where $\mathcal{D}_N$ is a linear operator on $\mathbf{x}'_k$ but depends on waves with wavenumbers other than k.

b. Procedure for forced linear model analysis

Our method is as follows. We first employ the forced linear model to reconstruct the planetary wave response obtained in the nonlinear simulation [i.e., $\mathbf{X} = \overline{\mathbf{x}}$ and $\mathbf{F}_k = \mathcal{N}(\mathbf{x}')_k$]. The ability to reconstruct the stratospheric planetary wave response is then tested in a series of forced linear model experiments in which we modify the basic state $\overline{\mathbf{x}}$ and the nonlinear forcing $\mathcal{N}(\mathbf{x}')_k$. In this way we are able to identify those aspects of $\overline{\mathbf{x}}$ and $\mathcal{N}(\mathbf{x}')_k$ that are most important to the planetary wave response in the stratosphere.

Before proceeding it is important to note a potential problem with the approach outlined above. In practice, the basic state $\mathbf{X}$ will be baroclinically unstable to all planetary-scale zonal wavenumbers in the troposphere—with growth rates increasing for increasing wavenumber, at least for small wavenumbers. Even in the special case where exact reproduction of the full nonlinear integration is attempted by taking $\mathbf{X} = \overline{\mathbf{x}}$ and $\mathbf{F}_k = \mathcal{N}(\mathbf{x}')_k$, unless $\overline{\mathbf{x}}$ and $\mathcal{N}(\mathbf{x}')_k$ are exactly as they were in the full nonlinear integration (i.e., to machine precision, extracted at every time step from the nonlinear model), small errors in the response might be expected to project onto unstable modes. The exponential growth of the unstable modes would quickly dominate the response and invalidate the procedure.

From a series of forced linear model experiments, it was found possible to perform 400-day integrations of either wave-1 or 2 without exciting baroclinic instability so long as $\mathbf{X}$ is prescribed to be the fully time-evolving $\overline{\mathbf{x}}$. Integrations with larger zonal wavenumbers (≥ 3) generally become dominated by baroclinic instability within several hundred days and we have not considered these. For the case when $\mathbf{X}$ is time independent (e.g., corresponding to the time-mean zonal-mean flow in the nonlinear simulation) we have found that wave-2 becomes dominated by baroclinic instability during the 400-day integration of the forced linear model. In order to suppress the instability of wave-2 during such time-independent $\mathbf{X}$ integrations of the forced linear model, we strengthened the Rayleigh surface friction above that used during the corresponding nonlinear integration and included Newtonian cooling near the surface.

All forced linear model experiments are integrated for 400 days. In order to quantify the difference in the response between experiments, we correlate time series of geopotential height amplitude for each zonal wavenumber. The correlations are evaluated at each grid point in the model domain corresponding to the intersection of model levels and Gaussian latitudes. A single representative measure of the correlation for each wavenumber between any two experiments is obtained by averaging the correlation coefficients over the lower stratosphere where the response is of primary interest (i.e., 30°, 70° latitude and 20, 40 km). Unless otherwise stated, the correlation is evaluated over the full 400-day integration.

c. Forced linear model experiments

In Table 1 we present the results from a series of forced linear model experiments. In the first experiment (F1) we attempt to reconstruct the full response in the nonlinear simulation by employing the time-evolving basic state $\mathbf{X} = \overline{\mathbf{x}}$ and complete nonlinear forcing $\mathbf{F}_k = \mathcal{N}(\mathbf{x}')_k$ up to an elevation of 50 km (above which it is decreased smoothly and rapidly to zero). In practice, we extract $\overline{\mathbf{x}}$ and $\mathcal{N}(\mathbf{x}')_k$ from the nonlinear simulation daily and smoothly interpolate between these values. In addition to being more practical, this sampling frequency also tests the utility of the method for sample rates that are typical of observations. The average correlation over the lower stratosphere between this experiment (F1) and the full nonlinear simulation (A0) is greater than 0.98 for both wave-1 and 2. This experiment demonstrates the ability of the forced linear model to reconstruct the planetary response of the the nonlinear simulation from the daily time series of $\overline{\mathbf{x}}$ and $\mathcal{N}(\mathbf{x}')_k$.

In the second experiment (F2) we investigate the source of variability of the planetary wave signal in the stratosphere. There are two possible sources of variability. One is the variability of the tropospheric eddy forcing $\mathcal{N}(\mathbf{x}')_k$. The other is the variability in the basic state $\overline{\mathbf{x}}$ through which the waves propagate. In order to determine the relative importance of the variability in $\overline{\mathbf{x}}$ versus the variability of $\mathcal{N}(\mathbf{x}')_k$, we perform a forced linear model integration (F2) in which we fix the basic state $\mathbf{X}$ to the time-mean (100–400 d) value of $\overline{\mathbf{x}}$. The geopotential height correlations for this experiment were calculated over the model period 100–400 d. The mean correlation of the stratospheric response in this experiment is 0.846 for wave-1 and 0.748 for wave-2.[1] These large correlations indicate that the time variation of the stratospheric planetary waves in the nonlinear simulation is governed primarily by the time variation of the nonlinear forcing $\mathcal{N}(\mathbf{x}')_k$ in the troposphere, and not by time variation of the basic state.

In the third experiment (F3) we repeat experiment F1 except that the nonlinear forcing $\mathcal{N}(\mathbf{x}')_k$ is imposed only up to 20 km (above which it is decreased smoothly and rapidly to zero). In this case the stratospheric response of waves-1 and 2 have correlation coefficients of 0.85

[1] As discussed in section 4b, the wave-2 integration of the F2 experiment required Newtonian cooling near the surface and enhanced Rayleigh friction near the surface in order to suppress baroclinic instability.

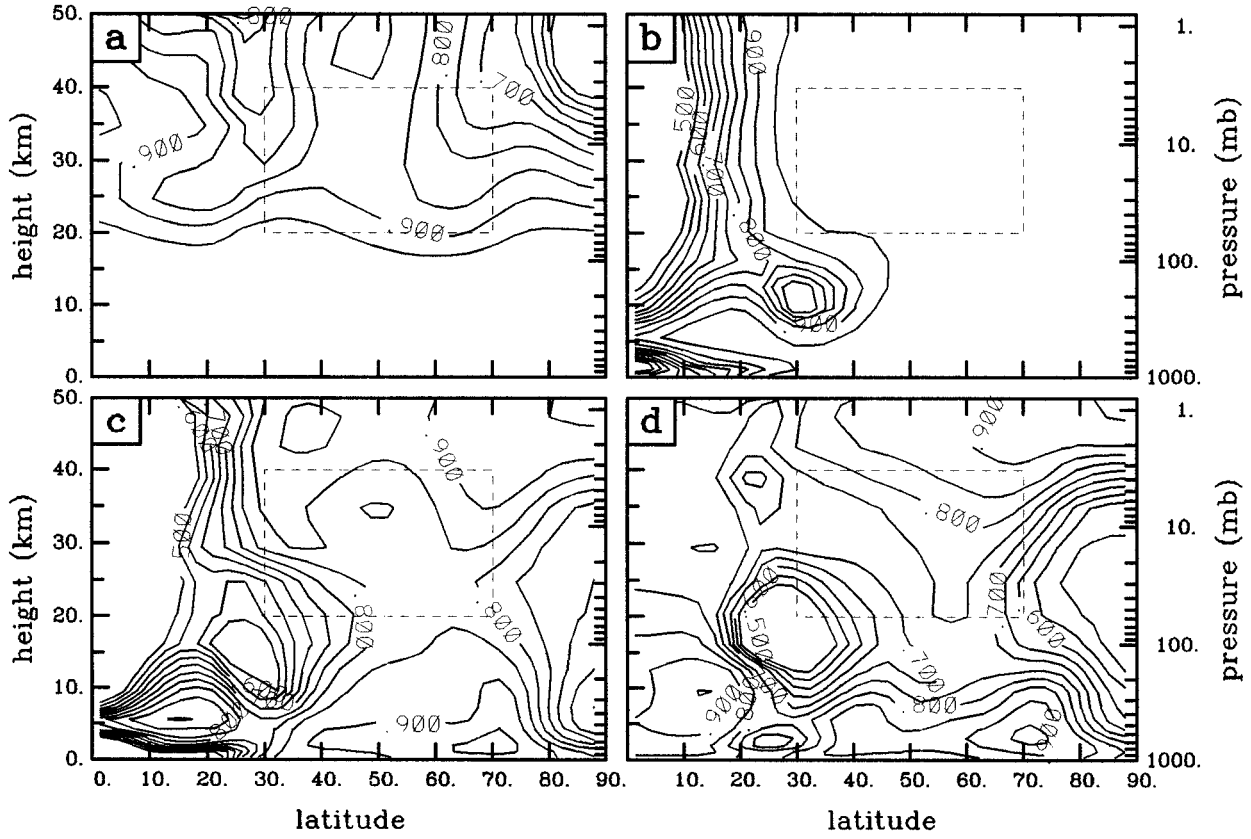

FIG. 9. Latitude–height plot of the correlation coefficient of wave-1 geopotential height amplitudes between the forced linear model experiment F3 and (a) the full nonlinear simulation A0, (b) experiment F4, (c) experiment TFD1, and (d) experiment TFD2. The box indicated by the dashed line represents the region of stratosphere over which the correlation coefficients were averaged for Table 1.

when compared to the full nonlinear simulation (A0). In Figs. 9a and 10a the correlation coefficient between the full run A0 and the experiment F3 are displayed as a function of height and latitude for waves-1 and 2, respectively. Over the depth that the nonlinear forcing $\mathbf{F}_k = \mathcal{N}(\mathbf{x}')_k$ is imposed ($\leq$20 km), the response of the forced linear model is nearly exact. This is also the case when the forcing is allowed to extend up to 50 km (experiment F1). In the forced linear model, experiments described in the remainder of this section show the forcing is applied only up to 20-km elevation.

The mean stratospheric correlation of geopotential height amplitudes decreases only slightly when the nonlinear forcing $\mathcal{N}(\mathbf{x}')_k$ is removed from the stratosphere (i.e., experiments F3 and F1). The large mean stratospheric correlations for experiment F3 imply that there is only weak nonlinearity in the stratosphere of the full nonlinear experiment (A0). This suggests that there is only weak wave breaking and hence weak wave-induced variability of the zonal-mean flow (this is evident in Fig. 16, discussed in section 6b). This is consistent with the result from experiment F2, which indicated that zonal-mean flow variability played a relatively minor role in the production of stratospheric planetary wave variability.

In all the first three forced linear model experiments we have imposed the eddy forcing $\mathbf{F}_k = \mathcal{N}(\mathbf{x}')_k$ in all the prognostic equations (i.e., vorticity, divergence, temperature, and surface pressure). However, the planetary wave response in the stratosphere is expected to be balanced and, as a consequence, its dynamics should be determined by the potential vorticity (hereafter PV) of the flow (e.g., Hoskins et al. 1985). Therefore, the only dynamically relevant component of the eddy forcing should be that which affects, or forces, the PV. This idea is most simply stated in the context of quasigeostrophic (QG) flow. Quasigeostrophic flow is balanced in the sense that all prognostic fields may be derived exactly from a single scalar field—the QG potential vorticity. The effect of the eddy forcing may be contained entirely within an eddy-forcing term in the QG potential vorticity equation. This forcing term may be expressed at leading order, under QG scaling, as a combination of the eddy vorticity and eddy temperature fluxes (see section 5a, where this is explicitly illustrated), and it is this combination of eddy forcings alone that is relevant.

Even though the flow in the model is outside of the strict regime of applicability of QG theory, it is arguable, since Rossby numbers at midlatitudes are not too large, that it is only the eddy vorticity and eddy tem-

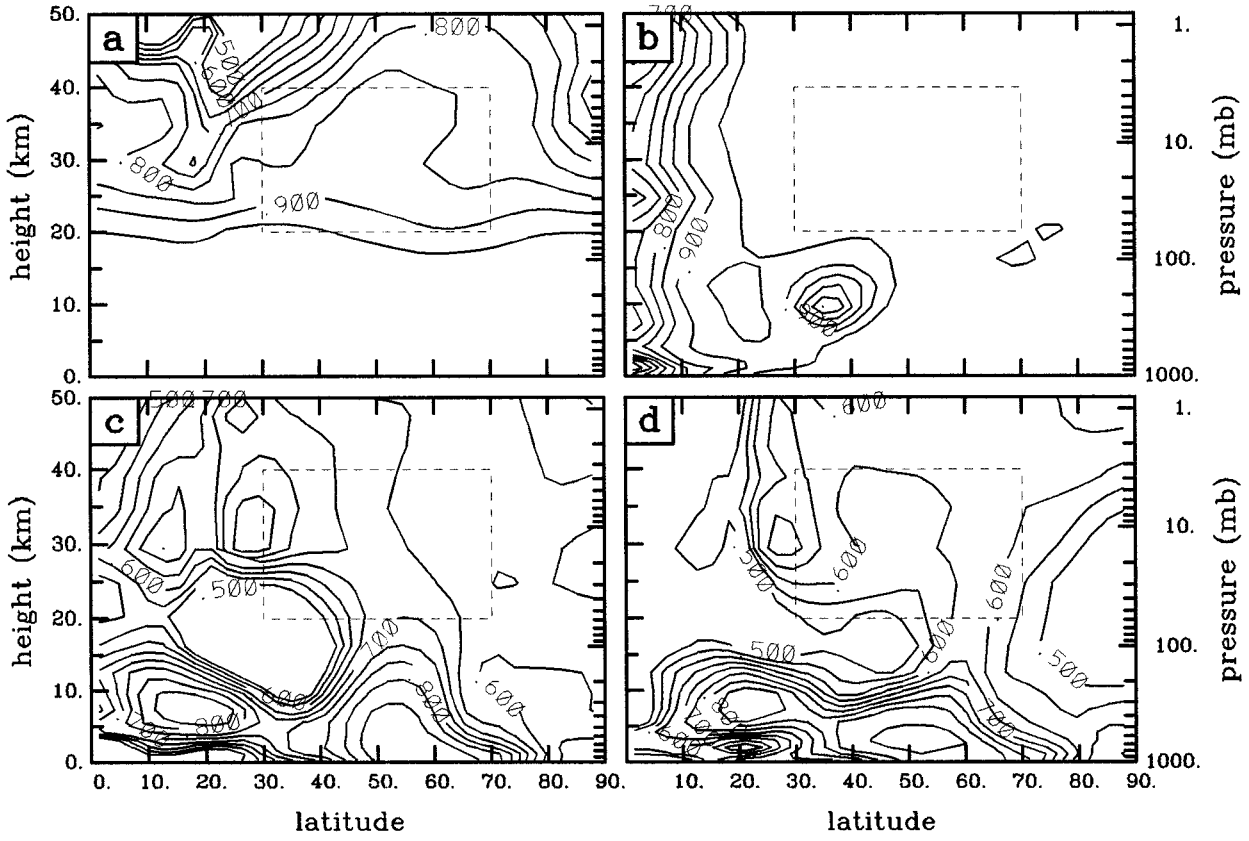

FIG. 10. Latitude–height plot of the correlation coefficient of wave-2 geopotential height amplitudes between the forced linear model experiment F3 and (a) the full nonlinear simulation A0, (b) experiment F4, (c) experiment TFD1, and (d) experiment TFD2. The box indicated by the dashed line represents the region of stratosphere over which the correlation coefficients were averaged for Table 1.

perature forcing fields that give the major part of the stratospheric planetary response. In order to test this, in a new forced linear model experiment (F4) we apply only the eddy vorticity and eddy temperature forcing (i.e., we remove the eddy forcing of both divergence and surface pressure). Compared to the experiment in which all eddy-forcing terms were retained (F3), this new experiment has a mean stratospheric correlation of greater than 0.97 for both waves-1 and 2. Figures 9b and 10b display the correlation coefficient between experiment F4 and experiment F3 as a function of height and latitude for waves-1 and 2, respectively. In Figs. 9b and 10b it is clear that poor correlations occur only at low latitude where simple ideas of balance, based on QG theory, break down.

We have performed two further experiments in which eddy forcing is retained in only the vorticity (F5) and temperature (F6) equations (see Table 1). The experiment that employs only vorticity forcing (F5) reproduces a significant portion of the wave-1 stratospheric response of the full experiment (A0). The experiment that employs only temperature forcing (F6) produces a response that is more poorly correlated with the full experiment (A0). These experiments indicate that both eddy-forcing fields are required for the adequate reconstruction of the stratospheric response in A0, although the contribution from the eddy-vorticity forcing is somewhat larger for wave 1.

The spatial structure of the nonlinear eddy forcing of vorticity and temperature are displayed in Figs. 11 and 12, respectively. Prior to plotting, we apply a 15-day low-pass time filter to the eddy-forcing fields (see discussion below regarding forced linear model experiments T1 and T2, which employ temporally filtered eddy forcing). In both figures, panels a and c correspond to wave-1 while panels b and d correspond to wave-2. Panels a and b of these two figures display the rms amplitude (in latitude) of the nonlinear eddy forcing as a function of height and time. Panels c and d of Figs. 11 and 12 display the amplitude of the nonlinear eddy forcing at approximately 10 km as a function of latitude and time.

It is clear from Figs. 11 and 12 that the meridional structure of the eddy forcing is more complicated than the vertical structure. In the vertical, both the the eddy vorticity forcing (Figs. 11a,b) and eddy temperature forcing (Figs. 12a,b) display a single extrema at about tropopause level. The eddy temperature forcing also displays some power near the surface (Figs. 12a,b). In the meridional direction, the eddy vorticity forcing (Figs.

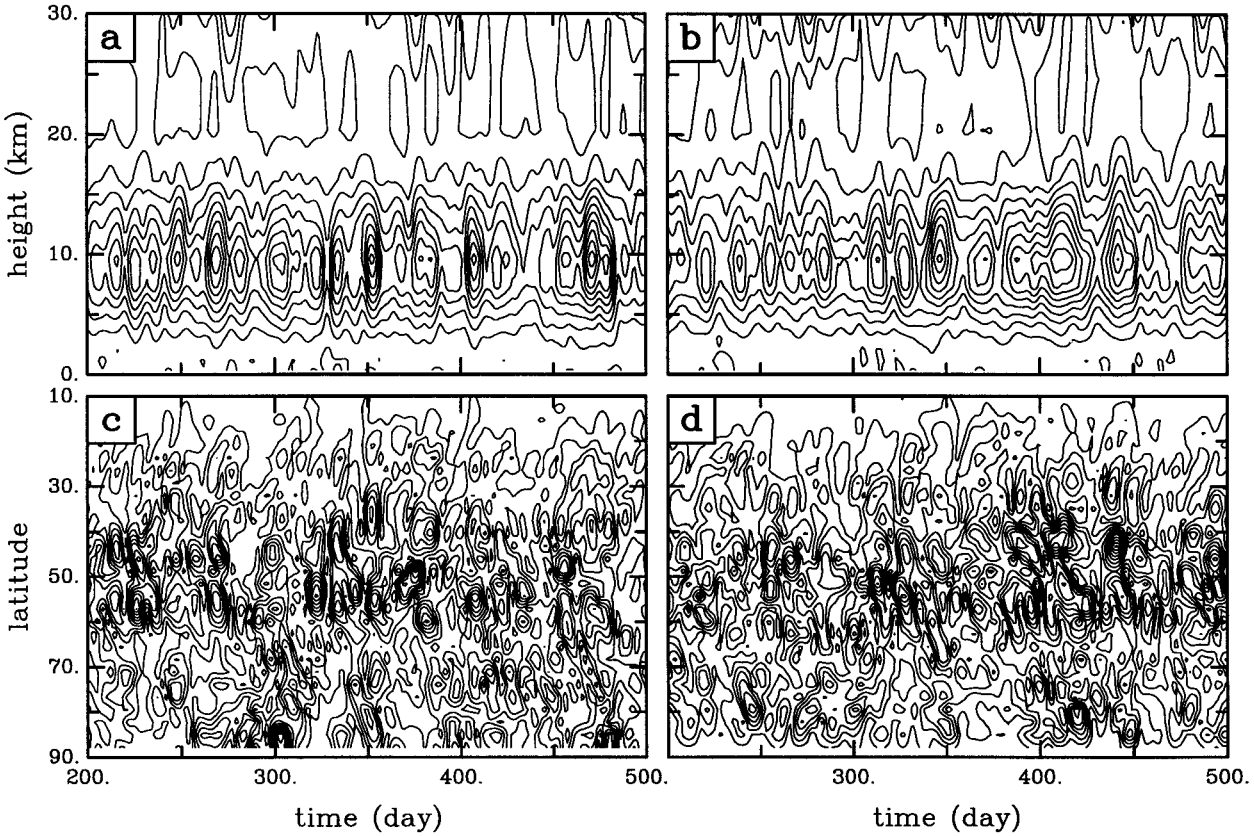

FIG. 11. (a), (b) Time–height plots of the rms (in latitude) amplitude of eddy vorticity forcing F_k^{ζ} for waves-1 and 2. (c), (d) Time–latitude plots of the amplitude of F_k^{ζ} for waves-1 and 2 near 10-km elevation.

11c,d) appears rather complicated and extends over a large range of latitudes. The meridional distribution of the eddy temperature forcing (Figs. 12c,d) appears to have two maxima, one on each side of the core of the time-mean tropospheric jet (e.g., see Fig. 18a).

A series of forced linear model experiments were undertaken to investigate the importance of the vertical and meridional structure of the eddy-forcing fields displayed in Figs. 11 and 12. In order to determine if the eddy temperature forcing near the surface made any contribution to the stratospheric response in the nonlinear experiment A0, we performed a forced linear model experiment (F7) similar to F6 in which the vertical profile of eddy temperature forcing Figs. 12c,d) is smoothly adjusted toward zero near the surface. This was accomplished by windowing the forcing with the factor $\{1 - \exp[-(z/4\text{ km})^2]\}$. The mean stratospheric correlation of this experiment (F7) with F6 is greater than 0.925 for both waves-1 and 2. This implies that the eddy temperature forcing near the surface (displayed in Figs. 12a,b) has little influence on the stratospheric planetary wave response in the nonlinear experiment A0.

Panels a and b of Figs. 11 and 12 appear to suggest that the eddy vorticity and eddy temperature forcing might well be modeled by a vertically localized source near tropopause level. In order to investigate this question we perform several forced linear model experiments in which the vertical structure of the eddy forcing is replaced by the compact profile $\sin^2[\alpha(z)]$ centered on $z = 10$ km, where $0 \leq \alpha(z) \leq \pi$. The amplitude of the $\sin^2$ profile of forcing varies both in latitude and time and is determined by equating its vertical integral with the vertical integral of the eddy forcing from $z = 0$ to 20 km. In two experiments (V1 and V2) we employ two depths of the $\sin^2$ profile to represent the eddy vorticity forcing. Both experiments result in large correlations for waves 1 and 2 with experiment F5, where the full vertical structure of the eddy vorticity forcing was retained. These large correlations appear to be independent of the depth of the forcing. In this case we conclude that the vertical structure of the eddy vorticity forcing is most simply described by a localized source near tropopause level.

When the same experiment is performed with the eddy temperature forcing (V3), we obtain a poorer correlation with the experiment that retains the full vertical structure of the eddy temperature forcing (F6; see Table 1). This poorer result can be understood if one takes the view, argued earlier, that it is the contribution of the eddy temperature forcing to the eddy potential vorticity forcing that is most important. Under QG scaling, the eddy vorticity forcing enters directly into the eddy forc-

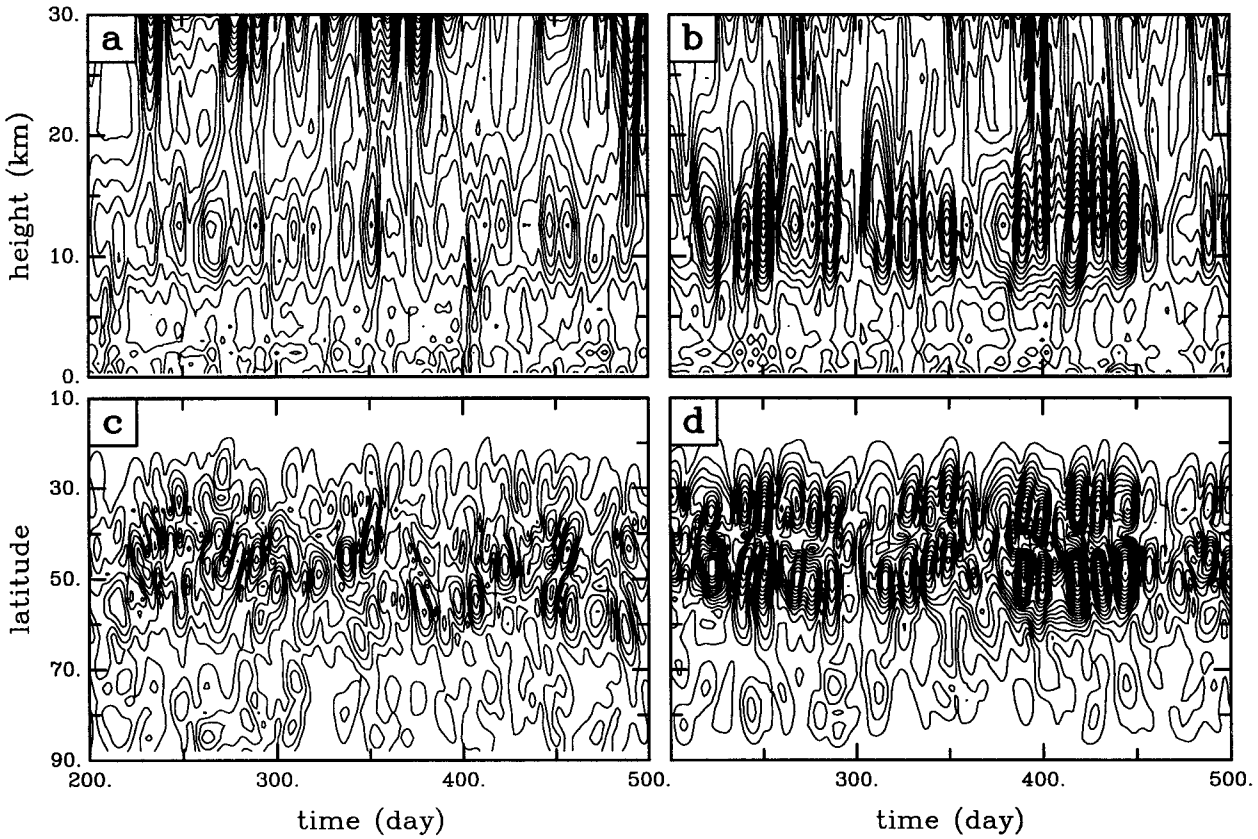

FIG. 12. (a), (b) Time–height plots of the rms (in latitude) amplitude of eddy temperature forcing F_k^T of waves-1 and 2. (c), (d) Time–latitude plots of the amplitude of F_k^T for waves-1 and 2 near 10-km elevation.

ing of QG PV, while the eddy temperature forcing enters primarily under a vertical derivative operator [e.g., the explicit form of the eddy forcing of QG PV is given by (15) in section 5a]. This implies that the planetary wave response should be sensitive to the details of the vertical structure of the eddy temperature forcing. Modeling the vertical structure of the eddy temperature forcing as a compact source (no matter how suggestive Figs. 12a,b) results in a response that is strongly dependent on the depth of the compact source selected (due to the strength of the implied vertical gradient).

In order to investigate the meridional structure of the eddy-forcing fields displayed in Figs. 11 and 12 (panels c and d), we perform several forced linear model experiments. In the first, the meridional structure of the eddy forcing of both vorticity and temperature is replaced by a Gaussian profile in latitude (see Table 1). The amplitude of the Gaussian forcing varies both in height and time and is determined by equating the meridional integral of the Gaussian forcing with the meridional integral of the eddy forcing. This experiment (M1) appears to be uncorrelated with the same experiment in which the full meridional structure of the eddy forcing is retained (F4). This would indicate that the meridional structure of the eddy forcing is fundamental to the response obtained in the stratosphere.

Figures 11 and 12 indicate that the eddy-forcing fields extend over a wide range of latitudes. In order to determine the contribution of the high- and low-latitude forcing to the stratospheric response, we perform experiments (M2 and M3) in which the eddy temperature and eddy vorticity forcing fields are windowed in the meridional direction. The window is a Gaussian that is centered near the latitude of time-mean tropospheric jet (45°) with half widths of 15° (experiment M2) and 25° (experiment M3). The mean stratospheric correlations with experiment F4 (taken over the period 100–400 days, see Table 1), in which the full meridional structure of the forcing is retained, are large for the widest window (M3). These large correlations indicate that the forcing at very high and very low latitudes is not fundamental to the stratospheric response.

In the previous section it was argued that, due to the filtering of upward-propagating planetary waves by the zonal-mean flow, rapid transience in the eddy forcing of planetary waves in the troposphere is unimportant to the planetary wave response in the stratosphere (see also section 6). By temporally filtering the eddy-forcing fields we can use the forced linear model to identify a ''cutoff'' timescale such that the eddy forcing associated with periods shorter than the cutoff have no effect on the response in the stratosphere. In two new forced lin-

ear model experiments we repeated experiment F4 using low-pass time-filtered representations of the eddy-forcing fields. In the frequency domain, the low-pass time filter was taken as the window $\{1 - \tanh[(\omega - \omega_0)/\omega_h]\}/2$ where $\omega_0 = 2\pi/P_0$ and $\omega_h = 2\pi/P_h$. In experiment T1 a 20-day low-pass filter is used (i.e., $P_0 = 20$ days and $P_h = 15$ days) and in experiment T2 a 15-day low-pass filter is used (i.e., $P_0 = 15$ days and $P_h = 15$ days). Both experiments provide large mean stratospheric correlations with the experiment that retained the full temporal structure of the nonlinear forcing. From these experiments one could define a cutoff timescale of 15–20 days. Therefore, in the full experiment A0, tropospheric eddy forcing associated with periods less than 15 days has little impact on the stratospheric planetary wave response.

5. Transformed Fourier decomposition

Both the eddy vorticity forcing and the eddy temperature forcing of the long waves [in Eq. (4)] are required to reproduce the stratospheric planetary wave response. This makes it difficult to characterize the structure of the eddy forcing of the long waves. For example, a detailed examination of each eddy-forcing field could be misleading since there may be significant cancellation in the combined response. A single representation of the eddy forcing is needed.

The same situation is encountered if one considers the eddy forcing of Eulerian mean (zonal-mean) flow. The Eulerian mean system, represented symbolically by (3), also requires only the eddy vorticity and eddy temperature forcing to determine the large-scale zonal-mean balanced response. However, it is well known that one can transform the Eulerian mean equations so that the eddy forcing of the zonal-mean vorticity and zonal-mean temperature are combined into one term. The new system is referred to as the transformed Eulerian mean (TEM) equations (e.g., Andrews et al. 1987).

In the first half of this section we derive a transformation of the equations that govern the Fourier amplitudes of deviations about the zonal-mean flow (4). The new system of equations combines the the eddy vorticity forcing F_k^{ζ} and eddy temperature forcing F_k^{T} of the long waves into a single eddy-forcing field. We refer to the new set of equations as the transformed Fourier decomposition (TFD) equations. The TFD equations are derived in analogy with the TEM transformation. In the second half of this section the TFD transformation is used to combine the eddy vorticity forcing and the eddy temperature forcing of the long waves. The spatial and temporal characteristics of the combined forcing is analyzed and used for several forced linear model integrations of the TFD system. It is helpful first to review the derivation of the TEM and TFD equations in their simplest form, which occurs for QG flow on a beta plane.

a. The TFD for QG flow on a beta plane

The QG vorticity, thermodynamic, and continuity equations for adiabatic and inviscid flow are, respectively,

$$\frac{\partial \zeta_g}{\partial t} + u_g\frac{\partial \zeta_g}{\partial x} + v_g\frac{\partial \zeta_g}{\partial y} + f_0 D_a = 0, \tag{6a}$$

$$\frac{\partial \theta_e}{\partial t} + u_g\frac{\partial \theta_e}{\partial x} + v_g\frac{\partial \theta_e}{\partial y} + w_a\theta_{0z} = 0, \tag{6b}$$

$$D_a + \frac{1}{\rho_0}(\rho_0 w_a)_z = 0, \tag{6c}$$

[e.g., Andrews et al. 1987, Eq. (3.3.3)] where $\zeta_g = v_{gx} - u_{gy} + f_0 + \beta y$ is the QG vorticity, D_a is the ageostrophic divergence, $\theta_e = \theta - \theta_0(z)$, $\theta_{0z}(z)$ is a reference potential temperature profile, the subscript g denotes geostrophic quantities, the subscript a denotes ageostrophic quantities, and the subscripts x, y, z denote differentiation in longitude, latitude, and height, respectively. All other quantities are defined in Andrews et al. (1987, chap. 3). For compactness of notation, we choose to work in terms of potential temperature θ in this discussion of QG flow but will use temperature T once again when we return to the primitive equations.

Decomposing $\{u_g, v_g, \zeta_g, \theta_e\}$ into a zonal mean (indicated by an overbar) plus deviation (indicated by a prime), and dropping the subscript g and e on all variables, the first two equations of (6) can be written

$$\frac{\partial \overline{\zeta}}{\partial t} + \frac{\partial \zeta'}{\partial t} + \overline{u}\frac{\partial \zeta'}{\partial x} + v'\frac{\partial \overline{\zeta}}{\partial y} + f_0 D_a = -\nabla\cdot(\mathbf{u}'\zeta'), \tag{7a}$$

$$\frac{\partial \overline{\theta}}{\partial t} + \frac{\partial \theta'}{\partial t} + \overline{u}\frac{\partial \theta'}{\partial x} + v'\frac{\partial \overline{\theta}}{\partial y} + w_a\theta_{0z} = -\nabla\cdot(\mathbf{u}'\theta'). \tag{7b}$$

Taking the zonal average and Fourier decomposition in longitude of (7) and (6c), respectively, results in

$$\frac{\partial \overline{\zeta}}{\partial t} + f_0\overline{D}_a = \overline{(u'v')}_{yy} \equiv \overline{F^{\zeta}}, \tag{8a}$$

$$\frac{\partial \overline{\theta}}{\partial t} + \overline{w}_a\theta_{0z} = -\overline{(v'\theta')}_y \equiv \overline{F^{\theta}}, \tag{8b}$$

$$\overline{D}_a + \frac{1}{\rho_0}(\rho_0\overline{w}_a)_z = 0, \tag{8c}$$

and

$$\frac{\partial \zeta_k'}{\partial t} + \overline{u}\frac{\partial \zeta_k'}{\partial x} + v_k'\frac{\partial \overline{\zeta}}{\partial y} + f_0 D_{ak} = -\{\nabla\cdot(\mathbf{u}'\zeta')\}_k \equiv F_k^{\zeta}, \tag{9a}$$

$$\frac{\partial \theta_k'}{\partial t} + \overline{u}\frac{\partial \theta_k'}{\partial x} + v_k'\frac{\partial \overline{\theta}}{\partial y} + w_{ak}\theta_{0z} = -\{\nabla\cdot(\mathbf{u}'\theta')\}_k \equiv F_k^{\theta}, \tag{9b}$$

$$D_{ak} + \frac{1}{\rho_0}(\rho_0 w_{ak})_z = 0, \tag{9c}$$

where the subscript k denotes the complex Fourier coefficient associated with longitudinal wavenumber k ($\neq 0$). Systems (8) and (9) are the QG representation of systems (3) and (4), respectively, which are discussed in section 4.

The transformation of (8) into the TEM equations follows three steps. First, the eddy forcing $\overline{F^\theta}$ in the thermodynamic Eq. (8b) is absorbed into a modified ageostrophic vertical velocity

$$\overline{w}_a^* \equiv \overline{w}_a - \overline{F^\theta}/\theta_{0z} = \overline{w}_a + (\overline{v'\theta'})_y/\theta_{0z}. \quad (10a)$$

Next, a modified ageostrophic divergence,

$$\overline{D}_a^* \equiv \overline{D}_a + \frac{1}{\rho_0}(\rho_0\overline{F^\theta}/\theta_{0z})_z = \overline{D}_a - \frac{1}{\rho_0}(\rho_0(\overline{v'\theta'})_y/\theta_{0z})_z, \quad (10b)$$

is defined from the continuity Eq. (8c) in order that no new eddy-forcing terms arise in that equation. Finally, the ageostrophic divergence $\overline{D}_a$ is eliminated from (8a) in favor of the modified divergence $\overline{D}_a^*$. As a consequence, the transformation from $\{\overline{D}_a, \overline{w}_a\}$ to $\{\overline{D}_a^*, \overline{w}_a^*\}$ results in a new set of (TEM) equations that, aside from boundary conditions, are isomorphic to (8a)–(8c) except that all of the eddy forcing has been concentrated to the right-hand side of the vorticity equation.

It is clear that the same type of transformation is possible for the system of Eq. (9), which governs the Fourier decomposition of deviations away from the zonal mean. The transformation is

$$w_{ak}^* \equiv w_{ak} - F_k^\theta/\theta_{0z} \quad (11a)$$

and

$$D_{ak}^* \equiv D_{ak} + \frac{1}{\rho_0}(\rho_0 F_k^\theta/\theta_{0z})_z. \quad (11b)$$

We will refer to the transformation (11) as the definition of the TFD for QG flow on a beta plane. As is the case for the TEM, aside from boundary conditions, the TFD system is isomorphic to the original system of equations (9) for that case in which all of the eddy forcing of wavenumber k is concentrated to the right-hand side of the vorticity Eq. (9a). The total effective eddy vorticity forcing of wavenumber k, which results from the TFD transformation, has the form

$$F_k^{\zeta+\theta} = F_k^\zeta + \frac{f_0}{\rho_0}(\rho_0 F_k^\theta/\theta_{0z})_z. \quad (12)$$

Inspection of (11) and (10) indicates that the form of the TEM and TFD transformations are identical, with the former acting on the zonal mean and the latter acting on all Fourier components. In this sense the effective vorticity forcing of the zonal-mean flow under TEM is the $k = 0$ component of (12). (The TEM equations are generally written in terms of horizontal velocities but may be re-expressed in terms of vorticity and divergence by differentiating the zonal and meridional momentum equations with respect to latitude.)

The extent to which the TEM and TFD transformations are successful in combining all relevant eddy forcing into one expression implicitly depends on the extent to which the dynamics they describe are balanced. By ''balanced'' we mean that the dynamics must be essentially governed by the evolution of one scalar field, PV say, and an inversion process whereby all other prognostic fields can instantaneously be recovered. If this is the case, then there must be a large set of right-hand sides for (9a) and (9b) that give the same balanced flow response. We may interpret the expression for total eddy vorticity forcing (12) as the the eddy vorticity forcing for the member of that set that has zero eddy temperature forcing. We might expect any eddy forcing that appears on the right-hand side of the perturbation equation for the scalar field to be completely determined (apart from functions of the mean state) by this total eddy vorticity forcing. [For more discussion on this point, in terms of forces rather than eddy-forcing terms, see McIntyre and Norton (1990).]

This is most easily illustrated for the case of QG flow since QG flow is governed by an exact underlying balance described by the material conservation of QG potential vorticity,

$$\frac{\partial q_g}{\partial t} + (\mathbf{u}_g \cdot \boldsymbol{\nabla}) q_g = 0, \quad (13)$$

where $q_g \equiv \zeta_g + (f_0/\rho_0)(\rho_0\theta_e/\theta_{0z})_z$. Decomposing the QG PV into a zonal-mean plus deviation in (13), and taking the Fourier decomposition in longitude of the resultant equation gives, when neglecting the subscripts g and e,

$$\frac{\partial q_k'}{\partial t} + \overline{u}\frac{\partial q_k'}{\partial x} + v_k'\frac{\partial \overline{q}}{\partial y} = -[\boldsymbol{\nabla}\cdot(\mathbf{u}'q')]_k \equiv F_k^q. \quad (14)$$

The total eddy forcing of the perturbation amplitude QG PV for wavenumber k can be written

$$F_k^q = -[\boldsymbol{\nabla}\cdot(\mathbf{u}'\zeta')]_k - \left[\frac{f_0}{\rho_0}(\rho_0\boldsymbol{\nabla}\cdot(\mathbf{u}'\theta')/\theta_{0z})_z\right]_k, \quad (15)$$

which in this case happens to be identical to the total effective eddy-vorticity forcing (12) derived from the TFD transformation.

b. The TFD for primitive equation flow

The TEM and TFD transformation of the zonal-mean primitive equations follows in a similar manner. The notable difference is that the primitive equations include a prognostic equation for divergence. As a consequence, the transformation from $\{\overline{D}, \overline{w}\}$ to $\{\overline{D}^*, \overline{w}^*\}$ and from $\{D_k, w_k\}$ to $\{D_k^*, w_k^*\}$ introduces additional eddy-forcing terms into the transformed divergence equation. Even if the response to such terms remains balanced, this is problematic from the point of view of attempting to combine all eddy forcing into one term [e.g., the effective vorticity forcing (12)]. However, the same problem arises in the TEM formalism and there the eddy-forcing terms for divergence

(or, equivalently, in the meridional momentum equation) are generally neglected on the basis that they are small in realistic parameter regimes (and disappear in the QG limit). We follow the same approach here for the TFD formalism, expecting that this approach is justified for at least the planetary-scale waves, where QG arguments might be expected to work best.

In the derivation of the TFD primitive equations, we first consider the set of prognostic equations that govern the Fourier decomposition of perturbations away from a zonally symmetric basic state [e.g., the explicit representation of Eq. (4) of section 3a]. For the numerical model employed here, the Fourier decomposed perturbation vorticity, temperature, and continuity equations are

$$\frac{D\zeta'_k}{Dt} + v'_k\frac{\partial\overline{\zeta}}{\partial\mu} + \zeta'_k\overline{D} + \overline{\zeta}\boldsymbol{D}'_k + \frac{1}{1-\mu^2}\frac{\partial}{\partial\lambda}\left[\overline{\dot{\sigma}}\frac{\partial v'_k}{\partial\sigma} + \dot{\boldsymbol{\sigma}}'_k\frac{\partial\overline{v}}{\partial\sigma} + (1-\mu^2)\left(\overline{T}\frac{\partial\,\overline{\ln p'_{*k}}}{\partial\mu} + T'_k\frac{\partial\,\overline{\ln p_*}}{\partial\mu}\right)\right]$$
$$-\frac{\partial}{\partial\mu}\left[\overline{\dot{\sigma}}\frac{\partial u'_k}{\partial\sigma} + \dot{\boldsymbol{\sigma}}'_k\frac{\partial\overline{v}}{\partial\sigma} + \overline{T}\frac{\partial\,\overline{\ln p'_{*k}}}{\partial\lambda}\right]$$
$$= \left[-\boldsymbol{\nabla}\cdot\left(u'\zeta' + \dot{\sigma}'\frac{\partial u'}{\partial\sigma} + (1+\mu^2)T'\frac{\partial\,\ln p'_*}{\partial\mu},\ v'\zeta' - \dot{\sigma}'\frac{\partial u'}{\partial\sigma} - T'\frac{\partial\,\ln p'_*}{\partial\lambda}\right)\right]_k \equiv F^{\zeta}_k, \tag{16a}$$

$$\frac{DT'_k}{Dt} + v'_k\frac{\partial\overline{T}}{\partial\mu} + \overline{\dot{\sigma}}\left(\frac{\partial T'_k}{\partial\sigma} - \frac{\kappa T'_k}{\sigma}\right) + \dot{\boldsymbol{\sigma}}'_k\left(\frac{\partial(T_0(\sigma)+\overline{T})}{\partial\sigma} - \frac{\kappa(T_0(\sigma)+\overline{T})}{\sigma}\right) + \kappa(T_0(\sigma)+\overline{T})\left(\boldsymbol{D}'_k + \frac{\partial\dot{\boldsymbol{\sigma}}'_k}{\partial\sigma}\right) + \kappa T'_k\left(\overline{D} + \frac{\partial\overline{\dot{\sigma}}}{\partial\sigma}\right)$$
$$= \left[\frac{-u'}{1-\mu^2}\frac{\partial T'}{\partial\lambda} - v'\frac{\partial T'}{\partial\mu} - \dot{\sigma}'\left(\frac{\partial T'}{\partial\sigma} - \frac{\kappa T'}{\sigma}\right) - \kappa T'\left(D' + \frac{\partial\dot{\sigma}'}{\partial\sigma}\right)\right]_k \equiv F^T_k \tag{16b}$$

$$\frac{D\,\ln p'_{*k}}{Dt} + v'_k\frac{\partial\,\overline{\ln p_*}}{\partial\mu} + \boldsymbol{D}'_k + \frac{\partial\dot{\boldsymbol{\sigma}}'_k}{\partial\sigma} = [-\mathbf{u}'\cdot\boldsymbol{\nabla}\ln p'_*]_k \equiv F^{\ln p_*}_k, \tag{16c}$$

where $D/Dt = \partial/\partial t + \overline{\mathbf{u}}\cdot\boldsymbol{\nabla}$, the overbar denotes a zonal mean, the prime denotes deviations away from the zonal mean, and the subscript k denotes the complex Fourier coefficient associated with longitudinal wavenumber k ($\neq 0$). The total temperature is $T = T_0(\sigma) + \overline{T} + T'$, where $T_0(\sigma)$ represents a reference temperature profile. All remaining notation can be found in Hoskins and Simmons (1975). The prognostic equation for the divergence D'_k is not included in (16) but is also required to complete the set of primitive equations [i.e., Eq. (4) of section 3a].

In the TFD transformation of 16, the components of divergence D'_k and vertical velocity $\dot{\sigma}'_k$ (highlighted in bold) are analogous to the components of ageostrophic divergence D_{ak} and vertical velocity w_{ak} in (9). In order that the transformation from $\{D'_k, \dot{\sigma}'_k\}$ to $\{D^{*\prime}_k, \dot{\sigma}^{*\prime}_k\}$ introduce no eddy forcing into the transformed continuity equation (16c) we require

$$D^{*\prime}_k + \frac{\partial\dot{\sigma}^{*\prime}_k}{\partial\sigma} = D'_k + \frac{\partial\dot{\sigma}'_k}{\partial\sigma}. \tag{17}$$

This is equivalent to the second step in the TEM transformation of the quasigeostrophic system (8).

The term $D'_k + \partial\dot{\sigma}'_k/\partial\sigma$ also appears in the thermodynamic equation (16b) but, because of the requirement (17), plays no role in the transformation of (16b). As a consequence, by analogy with the first step of the TEM transformation of (8), the eddy forcing in the thermodynamic equation (16b) can be absorbed into the modified vertical velocity

$$\dot{\sigma}^{*\prime}_k = \dot{\sigma}'_k - \frac{F^T_k}{\left(\dfrac{\partial\overline{T}}{\partial\sigma} - \dfrac{\kappa\overline{T}}{\sigma}\right)}. \tag{18a}$$

The transformed divergence $D^{*\prime}_k$ follows from (17) and is given by

$$D^{*\prime}_k = D'_k + \frac{\partial}{\partial\sigma}\left[\frac{F^T_k}{\left(\dfrac{\partial\overline{T}}{\partial\sigma} - \dfrac{\kappa\overline{T}}{\sigma}\right)}\right]. \tag{18b}$$

Finally, the divergence and vertical velocity $\{D'_k, \dot{\sigma}'_k\}$ are eliminated in favor of $\{D^{*\prime}_k, \dot{\sigma}^{*\prime}_k\}$ in the remaining equations. As discussed above, all eddy-forcing terms that arise as a result of the transformation in the prognostic equation for divergence are neglected. As a consequence, aside from boundary conditions, the TFD primitive equations are isomorphic to the original set (16) (including the divergence equation) for the case in which the system is forced solely through a modified

eddy vorticity forcing on the right-hand side of (16a). The modified vorticity forcing that arises from the TFD transformation is then

$$F_k^{\zeta+T} = F_k^{\zeta} + \overline{\zeta}\frac{\partial}{\partial\sigma}\left[\frac{F_k^T}{\left(\dfrac{\partial\overline{T}}{\partial\sigma} - \dfrac{\kappa\overline{T}}{\sigma}\right)}\right]. \tag{19}$$

In deriving $F_k^{\zeta+T}$ we have neglected eddy-forcing terms that arise from transforming $\dot{\sigma}_k'$ to $\dot{\sigma}_k^{*\prime}$ in (9a) since these were found only to have slight impact on the stratospheric planetary wave response. This is expected based on QG scaling [i.e., there is no term corresponding to $\dot{\sigma}_k'$ on the left-hand side of the QG vorticity equation (9a)].

Inspection of the TFD transformation of the primitive equations [(18) and (19)] and that of the QG equations [(11) and (12)] indicates close similarities. For example, in both systems the eddy temperature forcing enters the effective vorticity forcing through the vertical derivative of F_k^T divided by a measure of the static stability of the zonal-mean flow.

As is the case for the QG system, one can interpret the $k = 0$ component of the TFD transformation of the primitive equations as the prescription for a TEM-type transformation. In this case the transformation does not remove all the eddy-forcing terms in the temperature equation. But this is the case in the usual TEM equations too, where it it is usual practice to define the residual circulation $\{\overline{v}^*, \overline{w}^*\}$, so that some eddy terms are left on the right-hand side of the zonal-mean temperature equation [e.g., Andrews et al. 1987, Eq. (3.5.2e)]. Such eddy terms may be shown to be zero under ''nonacceleration'' conditions but, more importantly for our purposes, they are generally small in realistic parameter regimes. If these terms may be neglected then the $k = 0$ component of the TFD transformation [(18) and (14)] and the TEM form of the primitive equations are equivalent.

c. TFD forced linear model experiments

Aside from boundary conditions, the TFD equations are isomorphic to the the original system of equations (4) for the case in which the system is forced solely through the action of eddy vorticity forcing. Forced linear model integrations of the TFD system are performed by employing the original forced linear model (5) with the modified vorticity forcing $F_k^{\zeta+T}$ (9) in place of F_k^{ζ} and F_k^T.

In general, one must also modify the lower boundary condition from $\dot{\sigma}_k' = 0$ (zero normal flow) to $\dot{\sigma}_k^{*\prime} = -\{F_k^T/[(\partial\overline{T}/\partial\sigma) - (\kappa\overline{T}/\sigma)]\}_{\sigma=0}$ when employing (5) to integrate the TFD equations (see discussion above). However, from experiment F7 (Table 1) we have demonstrated that the stratospheric planetary wave response is insensitive to smooth adjustments of the vertical structure of F_k^T to set it to zero along the lower boundary. We will use this vertically rectified representation of F_k^T in the definition of the modified vorticity forcing $F_k^{\zeta+T}$ (9). As a consequence, we can retain the simpler lower boundary condition $\dot{\sigma}_k^{*\prime} = 0$ in forced linear model integrations of the TFD system.

Two forced linear model integrations of the TFD system are presented in Table 1. In the first experiment (TFD1) we apply the full modified vorticity forcing $F_k^{\zeta+T}$, which should be equivalent to experiment F4 (aside from slight differences, which are indicated by experiment F7, introduced by adjusting F_k^T to zero at the lower boundary). The mean stratospheric correlation of geopotential height fluctuations between experiment TFD1 and F4 is 0.88 for wave-1 and 0.73 for wave-2. The latitude–height distribution of the correlation coefficient between experiments TFD1 and F3 is displayed in Figs. 9c and 10c for wave-1 and wave-2, respectively.

One might imagine that the correlations of the TFD system with the untransformed system should be much closer to unity. However, as is the case for the TEM primitive equations, the TFD transformation of the primitive equations is based on the paradigm of QG balance. Therefore, the extent to which the TEM and TFD transformations are successful in combining all relevant eddy forcing into one expression implicitly depends on the extent to which the dynamics are described by QG balance (e.g., see discussion in section 5b above). It seems desirable to construct TEM and TFD transformations for systems representing higher orders of balance [see, e.g., the nonacceleration theorem derived for the semigeostrophic system by Kushner and Shepherd (1995)]. While such higher-order balanced formalisms have the promise of TEM and TFD transformations with improved accuracy, they also suffer from a significant increase in complexity.

In a second experiment (TFD2) the vertical structure of $F_k^{\zeta+T}$ is replaced by the compact profile $\sin^2[\alpha(z)]$ over the range 5–15 km, where $0 \leq \alpha(z) \leq \pi$. The amplitude of the $\sin^2$ profile of forcing varies both in latitude and time and is determined by equating its vertical integral with the vertical integral of $F_k^{\zeta+T}$ from $z = 0$ to 20 km. The large correlations between experiment TFD2 and TFD1 (Table 1) indicate that the total eddy forcing $F_k^{\zeta+T}$ is well modeled as a compact source located near tropopause level. The latitude–height distribution of the correlation coefficient between experiment TFD2 and F3 is displayed in Figs. 9d and 10d for waves-1 and 2, respectively.

The large correlations indicate that the TFD transformation has been largely successful in simplifying the eddy forcing down to one field. The spatial structure of the modified eddy vorticity forcing field $F_k^{\zeta+T}$ is displayed in Fig. 13. Consistent with experiments T1 and T2 (Table 1), a 15-day low-pass time filter is applied to $F_k^{\zeta+T}$ prior to plotting. Figures 13a,c display the time–height structure of the rms amplitude (in latitude) of $F_k^{\zeta+T}$ for waves-1 and 2, respectively. Figures 13b,d,

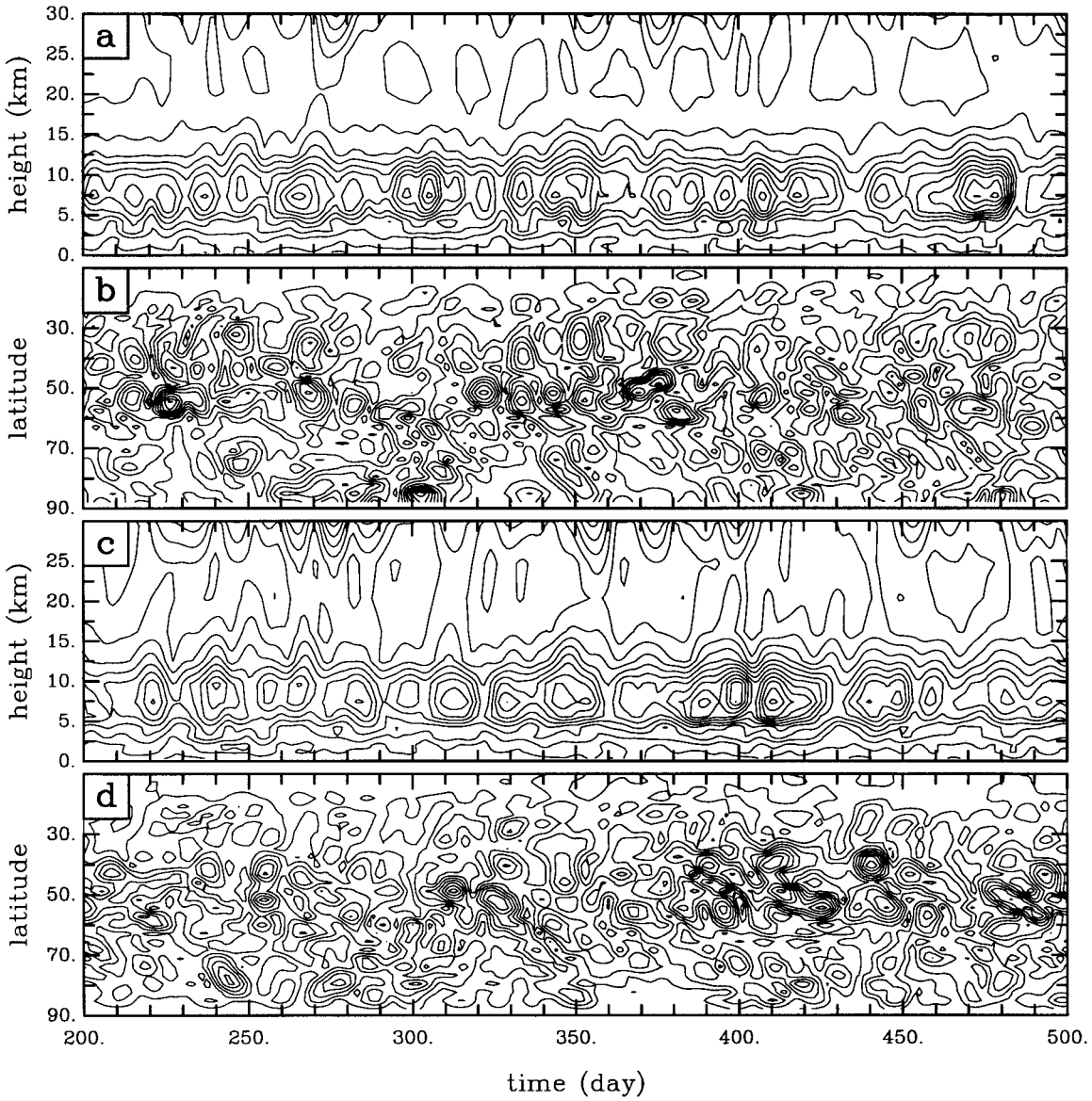

FIG. 13. Time–height plots of the rms (in latitude) amplitude of the total eddy forcing $F_k^{\xi+T}$, which results from the TFD transformation of waves-1 and 2. [(a) and (c)]. Time–latitude plots of the amplitude of vertically integrated $F_k^{\xi+T}$ for waves-1 and 2 [(b) and (d)]. For reference, contour intervals are identical to those employed for F_k^{ξ} in Fig. 11.

display the time–latitude structure of $F_k^{\xi+T}$ vertically integrated from 0 to 20 km. In the vertical, the total forcing of waves-1 and 2 display a single extrema that is localized about tropopause level. The meridional structure appears to be very complicated although we have already seen from forced linear model experiments M2 and M3 that the forcing present at very high and low latitudes contributes little to the response in the stratosphere.

In Fig. 14 we present the power spectra of the nonlinear eddy-forcing field $F_k^{\xi+T}$, vertically integrated from 0 to 20 km, as a function of frequency and latitude. Wave-1 is displayed in Figs. 14a,b and wave-2 is displayed in Figs. 14c,d. The full frequency spectrum is displayed in Figs. 14a,c, while the the 15-day low-pass filtered frequency spectrum is displayed in Figs. 14b,d. It is immediately apparent that the eddy forcing of wave-2 is dominated by a small band of rapid eastward propagation with periods ranging from 5 to 8 days. This range of periods is equivalent to the range of periods that characterized the packets of baroclinic eddies displayed in Figs. 7 and 8. It is clear then that, while the wave-2 packet organization of the baroclinic eddies imply strong nonlinear wave-2 forcing in the troposphere, the basic state does not support the propagation of disturbances with such large frequencies up into the stratosphere (see discussion of experiments T1 and T2 earlier in this section, and also section 6c). Figures 14b and

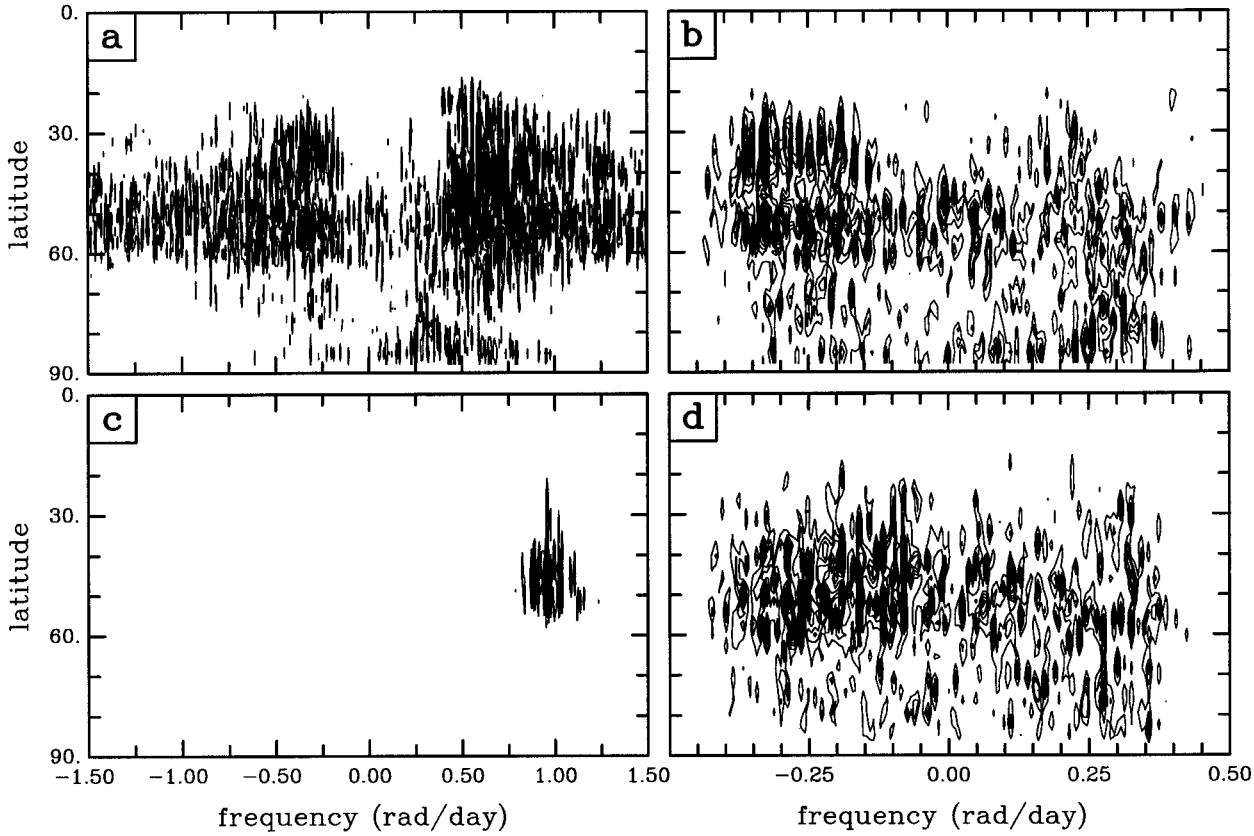

FIG. 14. Power spectra of total eddy forcing $F_k^{\zeta+T}$ of waves-1 and 2 as a function of frequency and latitude [(a), (c)]. The 15-day low-pass-filtered $F_k^{\zeta+T}$ for waves 1 and 2 [(b), (d)]. The strong high-frequency wave-2 forcing in (c) corresponds to the baroclinic wave packets illustrated in Figs. 7 and 8. For comparison, the contour intervals in (b) and (d) are half the value of those in (a) while those in (c) are 10 times the value in (a).

14d display the power of total eddy forcing of wave-1 and wave-2 over the narrow frequency range, identified by experiments T1 and T2, that is capable of influencing the stratosphere. The power of both waves-1 and 2 in Figs. 14b,d indicates that each is forced by the eddies in a roughly uniform manner over this range of frequencies.

6. Interpretation using linear wave calculations

While the stratospheric planetary response of the numerical simulation, presented in section 3b, displays some similarities with SH observations, there are significant quantitative and qualitative differences. One might imagine that the primary cause of such differences is the simplicity of the model troposphere (e.g., no topographic forcing, no diabatic forcing associated with land–sea temperature contrasts, etc.). However, many of the differences identified in section 3b can be argued to arise from differences of the zonal-mean basic state between the numerical simulation and observations.

Some examples of differences between the numerical simulation and SH observations are as follows. The stratospheric planetary response in the numerical simulation displays both eastward- and westward-traveling wave-2 whereas the observations indicate only eastward-traveling wave-2. The numerical simulation shows only low-frequency (20–100-day period) wave-2 disturbances whereas the observations indicate an additional high-frequency band with periods of 5–12 days. The upward group velocities for each wavenumber in the numerical simulation (inferred from Fig. 6) are slower than those observed for the SH. Finally, the maximum amplitudes of waves-1 and 2 in the numerical simulation are approximately half the value of those observed in the Southern Hemisphere. In this section, we apply simple linear wave theory, combined with forced linear model experiments, to investigate the dependence of the stratospheric planetary response on the zonal-mean basic state through which the waves propagate. We argue that each of the differences above may arise from the different linear wave propagation characteristics of the zonal-mean flow in the simulation as compared to that observed in the SH.

a. Application of Charney–Drazin theorem

For simplicity we consider forced planetary waves in quasigeostrophic flow on a beta plane, and we assume

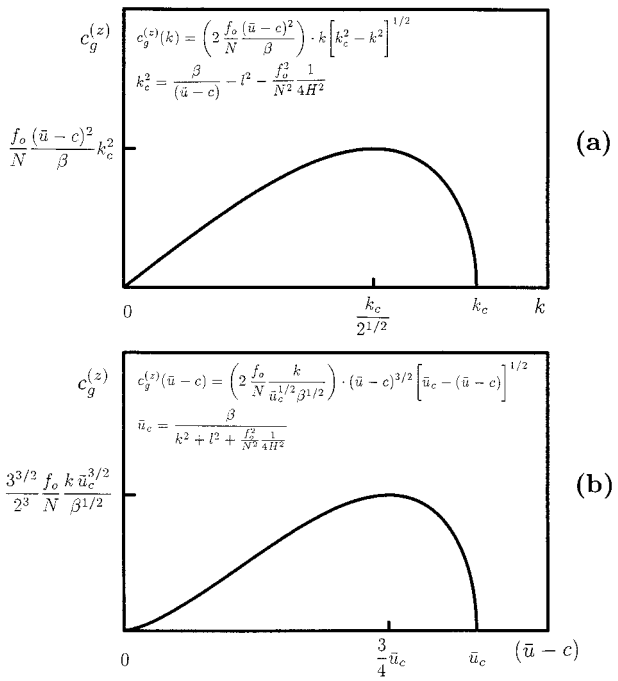

FIG. 15. Functional dependence of vertical group velocity $c_g^{(z)}$ on (a) the zonal wavenumber k and (b) the intrinsic phase speed for Rossby waves governed by quasigeostrophic flow on a beta plane for a basic state of constant wind $\overline{u}$ and static stability N^2.

slowly varying basic-state winds $\overline{u}$ and static stability N (e.g., Andrews et al. 1987, chap. 4.5.2). The Charney–Drazin theorem (1961) provides a condition on the phase speed c or frequency ω in order that propagating (wavelike) disturbances exist. These are

$$0 < \overline{u} - c < \overline{u}_c \tag{20}$$

and

$$k(\overline{u} - \overline{u}_c) < \omega < k\overline{u}, \tag{21}$$

where $\overline{u}_c \equiv \beta[k^2 + l^2 + f^2/(4N^2H^2)]^{-1}$ is the critical zonal mean wind, k and l are the zonal and meridional wavenumbers, f is the constant Coriolis parameter, N is the Brünt-Väisälä frequency, and H is the pressure-scale height.

In Fig. 15 we present the functional dependence of the vertical group velocity $c_g^{(z)}$ on the zonal wavenumber k and the negative intrinsic phase speed $(\overline{u} - c)$ for wavelike solutions that satisfy (20) and (21). Vertical wave propagation is possible only for a range of zonal wavenumbers and intrinsic phase speeds. Beyond a cutoff wavenumber k_c, or cutoff intrinsic phase speed $\overline{u}_c$, all disturbances are evanescent.

Within the bands $[0, k_c]$ and $[0, \overline{u}_c]$ the vertical group velocity $c_g^{(z)}$ displays a simple functional form. As either k or $\overline{u} - c$ is increased from zero the group velocity increases from a value of zero up to a maximum value located at $k = k_c/2^{1/2}$ and $(\overline{u} - c) = (3/4)\overline{u}_c$, respectively. Over the remaining portion, the vertical group velocity rapidly decreases toward zero. In both cases, the vertical group velocity is an increasing function over approximately three-quarters of the interval.

A quantitative application of Fig. 15 to the numerical simulation or to the observations is not a straightforward matter. However, Fig. 15 can be applied qualitatively to the numerical simulation and observations. For example, in section 3b we concluded from Fig. 6 that the cross-over zonal wavenumber for the transition from upward propagating to evanescent waves occurs near planetary wave 4 (i.e., k_c roughly corresponds to wave 4). This would indicate that wave-1 to wave-3 should fall roughly within the first three-quarters of the range $[0, k_c]$. As a consequence, we have the prediction that the vertical group velocity should be an increasing function over the first three wavenumbers. This is observed in the numerical simulation as well as in SH observations (Randel 1987). This simple explanation for the observed dependence of vertical group velocity on zonal wavenumber has strong appeal since it is not restricted to stationary waves.

The slower upward propagation of each wavenumber in the numerical simulation compared to SH observations can also be understood by applying the Charney–Drazin theorem (Fig. 15) to the results of the forced linear model simulations presented in the previous section. The total eddy forcing, previously presented in Figs. 14b and 14d, indicates that waves-1 and 2 are roughly evenly forced over the full range of frequencies that correspond to waves that can propagate up into the stratosphere. This corresponds to frequencies in the interval $[k(\overline{u} - \overline{u}_c), k\overline{u}]$ given by (21) or to intrinsic phase speeds in the interval $[0, \overline{u}_c]$ given by (20). Therefore, three-quarters of wave events necessarily come from the range $[0, (3/4)\overline{u}_c]$. As a result, an increase in the basic-state wind $\overline{u}$ should result in an increase in the vertical group velocity, measured over an ensemble of events, for each wavenumber. As was noted in section 3, the stratospheric winds in the SH winter stratosphere are roughly a factor of 2 stronger than those that develop in the numerical model. As a consequence, the slower upward propagation of waves-1 and 2 in the numerical simulation, compared to those observed in the SH (Randel 1987), is consistent with this simple application of the Charney–Drazin theorem.

b. Linear wave propagation characteristics of the time-mean flow

Much of the planetary wave response characterized in Figs. 4 and 5 can be understood in terms of the linear planetary wave propagation characteristics of the time-mean basic state. In Figs. 16a,c, we present contour plots of the time-averaged (100–400 day) meridional distribution of the vertical shear of the zonal-mean wind (in units of m s^{-1} km^{-1}) and the static stability (in units of 10^{-4} s^{-2}), respectively. In Figs. 16b,d, the rms deviation about the time averaged is displayed opposite each field.

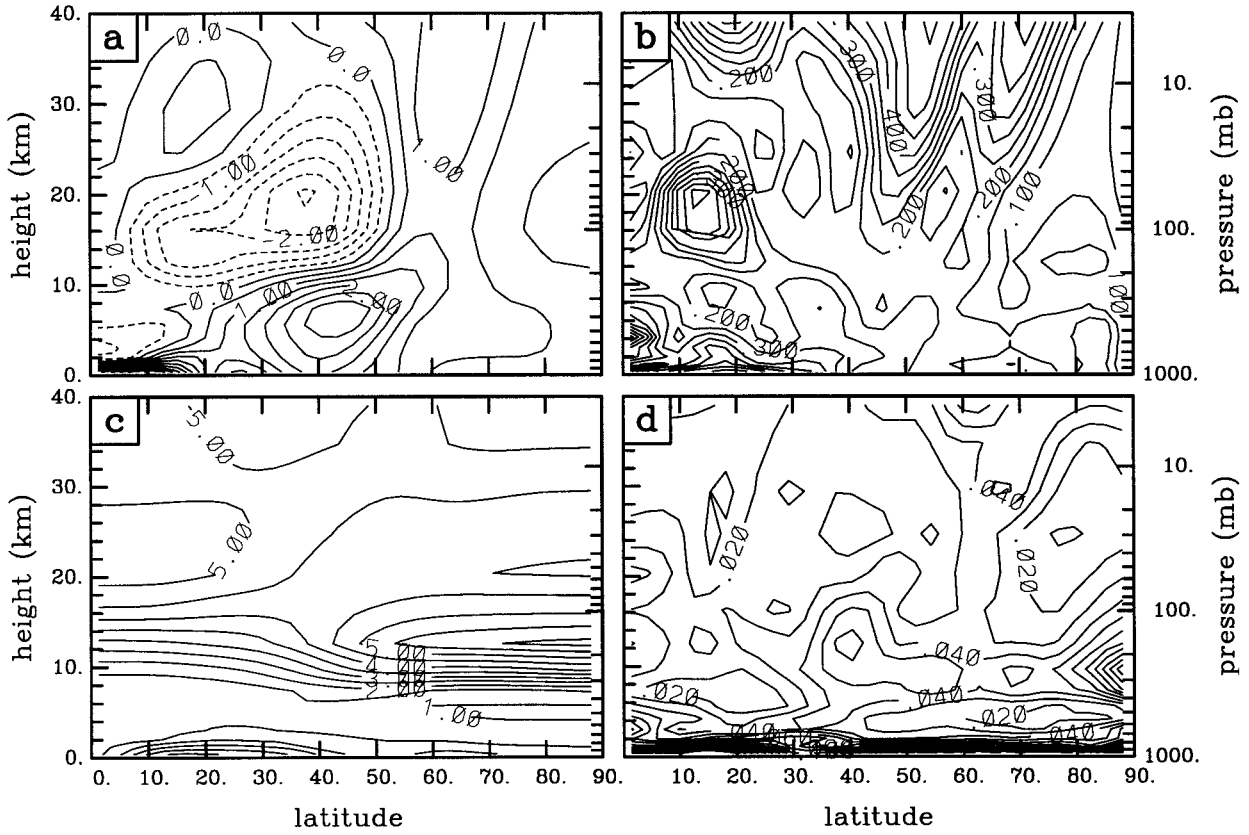

FIG. 16. (a) The vertical shear of the time-averaged (100–400 d) zonal-mean zonal wind and (b) its rms deviations from the time average; (c) the time-averaged zonal-mean static stability and (d) its rms deviations from the time average. Contour intervals are m s^{-1} km^{-1} for vertical wind shear and 10^{-4} s^{-2} for static stability.

It is clear from Figs. 16b,d that the time-mean basic state displays weak variability (5%–20% in the upper troposphere/lower stratosphere). The time-averaged basic state, therefore, is a good representation of the flow through which planetary-wave disturbances propagate in the numerical simulation. This is supported by the forced linear model experiment F2 (Table 1), which indicates that the stratospheric response is relatively insensitive to the temporal variability present in the zonal-mean flow.

In order to identify the planetary-wave propagation characteristics of the time-averaged basic state, we undertake a set of forced linear model experiments with an idealized tropospheric vorticity forcing $\mathbf{F}_k = F_k^{\zeta}$ in (5). In all experiments the vorticity forcing takes the form

$$F_k^{\zeta} \propto \sin(z\pi/10 \text{ km}) \sin[2\pi(\phi - 20°)/40°] \exp^{-i\omega t},$$

$$0 \le z \le 10 \text{ km}, \qquad 20° \le \phi \le 60°, \qquad 0 \le t,$$

where $\omega = 2\pi/P$ is the frequency of the forcing and P its period.

In a series of experiments we consider the response of waves 1–4 to this forcing with periods that range from -100 to 100 days. The integrations are carried out to 50 days. For the purpose of comparison, the amplitude of the forcing is held constant in all experiments. In order that the response in each case becomes steady by the end of the integration we apply Rayleigh friction and Newtonian cooling near the lower boundary. A relaxational timescale of 0.5 day is employed at the surface for both forces and the Rayleigh friction and Newtonian cooling decay exponentially in the vertical with *e*-folding depths of 1 and 2 km, respectively.

Figure 17 presents a summary of all of these experiments. In this figure the final meridionally integrated upward E–P flux at 30-km elevation is plotted as a function of the frequency ω of the imposed forcing F_k^{ζ} for waves 1–4. For reference, the midlatitude phase speed for each experiment is indicated at the top of the figure (note that the numerical values of the midlatitude phase speed have been multiplied by the zonal wavenumber index *n,* which results in a single representative number at each frequency).

Figure 17 is consistent with the analysis of the nonlinear simulation A0 and with the results of the forced linear model experiments presented in section 4. It indicates that upward propagation is only possible for a band of low frequencies. This is consistent with the

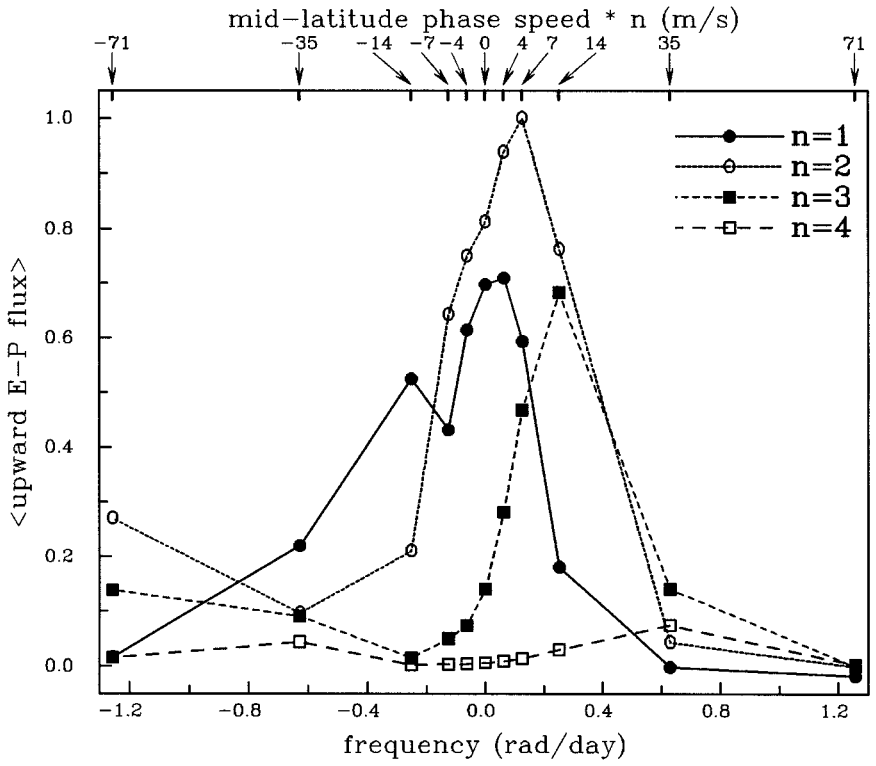

FIG. 17. Summary of forced linear model experiments that employed idealized vorticity forcing. The final latitudinally integrated upward E–P flux is displayed for waves 1–4 from a series of experiments in which the period of the vorticity forcing is varied from −100 to 100 days. For reference, the midlatitude phase speed (multiplied by the zonal wavenumber index n) associated with each experiment has been indicated along the top of the plot.

forced linear model experiments T1 and T2 (see Table 1) and with the Charney–Drazin theorem as described above.

The dependence of upward E–P flux on the frequency, for each zonal wavenumber, appears to be consistent with the simple application of the Charney–Drazin theorem discussed above and summarized in Fig. 15. From (21), we expect upward-propagating waves over the range of frequencies $[\omega_{\text{low}}, \omega_{\text{high}}]$, where $\omega_{\text{low}} = k(\overline{u} - \overline{u}_c)$ and $\omega_{\text{high}} = k\overline{u}$. As k is increased, ω_{low} and ω_{high} both shift to higher frequency (i.e., toward eastward propagation). This explains the shift of the peak upward E–P flux toward positive frequencies in Fig. 17 as the zonal wavenumber k is increased. This effect would also seem to explain the tendency for the stratospheric response to be skewed toward more negative frequencies (westward propagation) for wave-1 and more positive frequencies (eastward propagation) for wave-2 in Figs. 4c and 4d.

In a similar manner, as $\overline{u}$ is decreased, both ω_{low} and ω_{high} shift toward more negative frequencies (westward propagation). As a consequence, we would expect stronger westward propagation, of each wavenumber, in the numerical simulation compared to the SH observations since the effective $\overline{u}$ is weaker in the numerical simulation. This helps account for the presence of westward-propagating wave-2 in the numerical simulation compared to its relative absence in SH observations (see discussion regarding Fig. 4d in section 3).

c. *Higher-frequency component of stratospheric planetary-wave response*

The wave-2 experiments illustrated in Fig. 17 indicate that the time-mean zonal-mean flow that develops in the numerical simulation does not strongly support upward-propagating waves with frequencies greater than about 0.6 rad day^{-1} (periods less than 10 days). When the actual eddy forcing was employed in the forced linear model, it was found that frequencies greater than 0.4 rad day^{-1} (periods less than 15 days) had little influence on the stratospheric response (e.g., experiments T1 and T2 of Table 1). It is clear from Fig. 14c, however, that the tropospheric eddy forcing of wave-2 in the numerical simulation is strongest at the higher frequencies of 0.8–1.2 rad day^{-1} (periods of 8–5 days). This higher-frequency forcing appears to be directly related to the dominant characteristics of the packet structures of the baroclinic eddies (see discussion in section 3c).

In this section, we consider the effect that stronger basic-state winds have on the upward propagation of the higher-frequency transience associated with the bar-

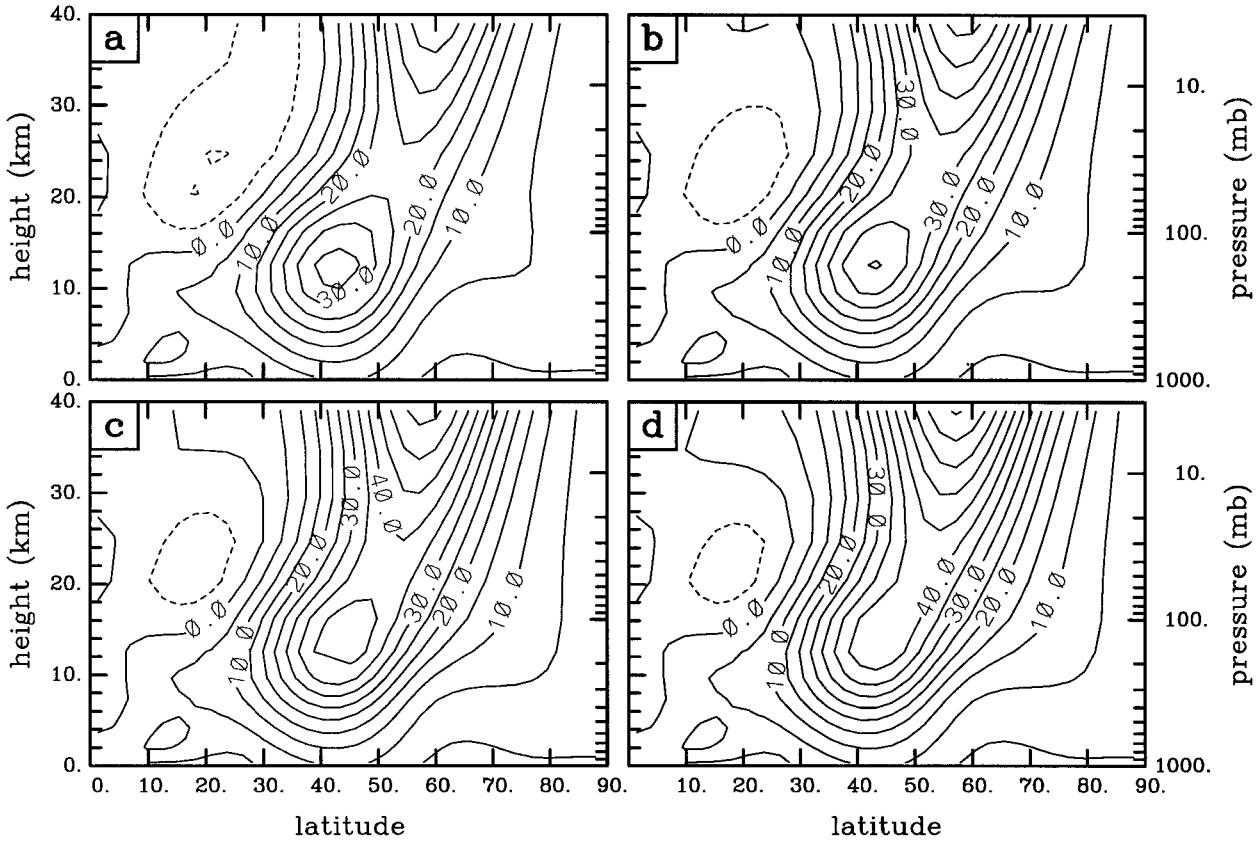

FIG. 18. Basic-state zonal winds used in four new forced linear model experiments. (a) Time-averaged (100–400 d) zonal mean from the numerical simulation. (b)–(d) The time-averaged zonal mean modified by small enhancements of the stratospheric wind.

oclinic wave packets. The stratospheric response of the numerical simulation indicated only low-frequency (e.g., periods greater than 15 days) wave-2 disturbances. Southern Hemisphere observations, on the other hand, indicate an additional, higher-frequency band [with periods ranging from 5 to 12 days, Manney et al. (1991)]. One possibility is that the stronger basic-state SH winds allow the upward propagation of the higher-frequency transience forced directly by the packets of baroclinic eddies, and that this accounts for the higher-frequency band of wave-2 disturbances observed in the SH stratosphere (i.e., ω_{low} and ω_{high} shift toward positive frequencies when $\overline{u}$ increases).

These ideas are examined by performing several new forced linear model experiments. In all these experiments the forcing is specified as the eddy vorticity and eddy temperature forcing derived from the full nonlinear simulation A0 and is imposed up to 20-km elevation. The basic state of the forced linear model is fixed to the time-mean zonal-mean flow derived from A0 (i.e., $\mathbf{X} = \overline{\mathbf{x}}$). In a series of experiments we adjust the strength of the stratospheric winds in the time-mean basic state. This is achieved by adding to the time-mean winds a localized disturbance wind U_{pert}. In practice we employ the stratospheric part of the expression for basic-state zonal wind defined in the appendix giving

$$U_{\text{pert}} = G(\phi)[U_{\text{strat}}(z)F_{\text{strat}}(\phi)], \tag{22}$$

where all terms are defined in the appendix. As described in the appendix, the definition of $U_{\text{strat}}(z)$ is designed to prevent U_{pert} from altering the vertical wind shear near the surface. Four experiments are performed where all parameters in (22) are identical to those specified in the appendix except for $\{U_{0s}$ (m s^{-1}), c_1 (km)$\}$ $= \{0, —\}$, $\{30, 34\}$, $\{30, 50\}$, and $\{50, 40\}$. Here, U_{0s} is the local maximum, and c_1 the vertical half width, of the perturbation to the zonal wind. The zonal wind fields, respectively corresponding to each of these experiments, are displayed in Figs. 18a–d.

Each forced linear model experiment is integrated for 1050 days in order to obtain high-resolution frequency spectra of the stratospheric response, equivalent to those previously displayed in Figs. 4c,d. In order to suppress baroclinic instability, we employed the enhanced surface friction and thermal damping described above in section 5b. The additional tanh factor in the definition of $U_{\text{strat}}(z)$ (see the appendix) prevents U_{pert} from altering the vertical wind shear near the surface and, hence, the criticality of each flow in the troposphere. As a consequence, waves-1 and 2 were stable during the entire integration of the forced linear model in each of the four experiments.

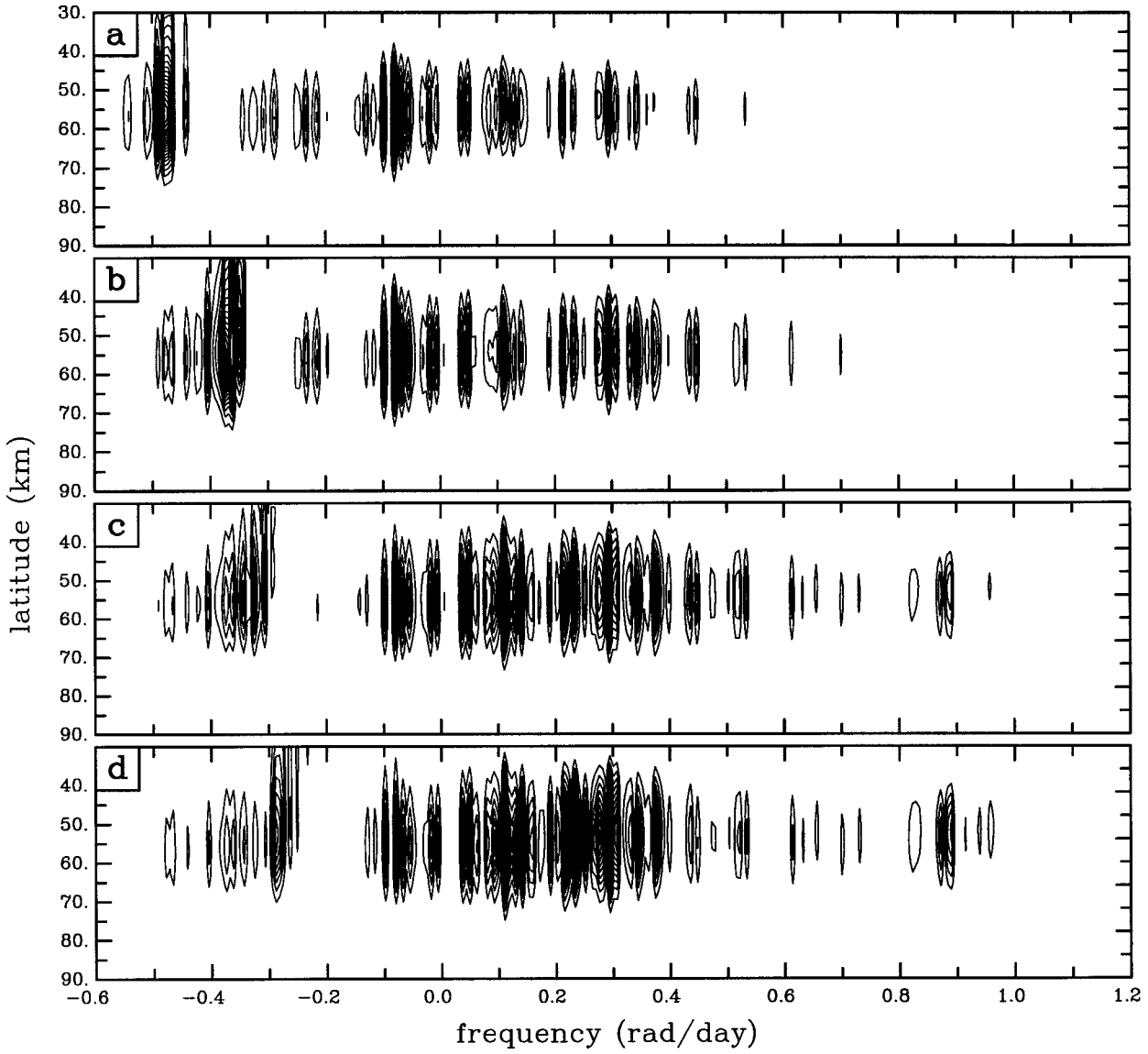

FIG. 19. (a)–(d) Frequency–latitude power spectra of wave-2 geopotential height amplitude on the 10-mb pressure surface from four forced linear model experiments. The basic-state wind field used in each experiment is respectively displayed in Fig. 18.

In Fig. 19 we present the frequency spectra of wave-2 geopotential height fluctuations, on the 10-mb pressure surface, which correspond to the four cases of basic-state zonal wind presented in Fig. 18. As the winds are increased in the lower stratosphere there are two obvious effects. One is the amplification of low-frequency disturbances (in the range -0.1 to 0.4 rad day^{-1}). This amplification illustrates the well-known tendency of increased geopotential height amplitudes in regions of stronger zonal wind (e.g., Simmons 1974). This provides the most obvious explanation for the factor of 2 difference in geopotential height amplitudes at 10 mb in the numerical simulation compared to SH observations (note that the observed SH wintertime zonal wind at 10 mb is a factor of 2 stronger than that in the numerical simulation, displayed in Fig. 18a, and still a factor of 1.5 stronger than the experiment with the most intense winds, Fig. 18d).

The other effect of increasing the basic-state wind is a shift in the response toward positive frequency (eastward propagation), as suggested by the simple application of the Charney–Drazin theorem outlined above. As the response shifts toward positive frequencies it begins to pick up the higher-frequency transience directly forced by the baroclinic wave packets.

These experiments confirm the expectation that stronger stratospheric winds will allow the higher-frequency transience associated with the packets of baroclinic eddies up into the stratosphere. This suggests that the higher-frequency wave-2 response observed in the Manney

et al. (1991) study may be directly forced by the dominant wave-2 structure of baroclinic wave packets observed in the SH troposphere (e.g., Lee and Held 1993; Berbery and Vera 1996). The lower-frequency stratospheric response is thought to be associated with more subtle aspects of the baroclinic wave packets such as their spatial and temporal variability, and this is discussed in the next section.

7. Discussion

In this study we have investigated the nature of stratospheric planetary-wave transience that develops solely as a consequence of forcing due to baroclinic eddies in the troposphere. In a long forced–dissipative numerical simulation it was found that such forcing could lead to realistic planetary-wave variability in the stratosphere.

The simple numerical experiment considered here was not designed with the intention of making detailed comparisons with observations. However, a comparison of the results with Southern Hemisphere stratospheric observations indicated that there are many qualitative similarities. Where differences do occur, many appear to be explained as arising from differences in the strength of the modeled and observed basic-state wind, which affects the propagation characteristics of the planetary waves (e.g., upward group velocity).

In order to investigate the the eddy-forcing mechanism in the numerical simulation, we developed a forced linear model designed to reproduce the stratospheric planetary response given the evolution of the zonal-mean flow and nonlinear eddy-forcing fields. The forced linear model was employed to determine those properties of the the eddy forcing that are essential for the reproduction of the stratospheric response.

By fixing the basic state of the forced linear model to the time-mean basic state of the nonlinear simulation it was demonstrated that the variability of the basic state had little impact on the reconstruction of the stratospheric planetary-wave response. Chen and Robinson (1992) have suggested that variability of the basic-state static stability and vertical wind shear at the tropopause could act as a ''valve'' for upward-propagating planetary waves, providing a source of planetary-wave transience in the stratosphere. This mechanism was essentially absent in the present numerical simulations due to the weak variability of the zonal-mean flow in the lower stratosphere. However, given that the important nonlinear forcing comes from a region about the tropopause, one might expect that the wave propagation characteristics of the flow at the level of the tropopause itself are not particularly significant.

The analysis of the forced linear model experiments indicated that both the eddy vorticity and eddy temperature forcing fields from the full numerical simulation were required for the adequate reconstruction of the stratospheric response of each planetary wave. This is consistent with the fact that the planetary waves, which make up the transient disturbances in the stratosphere, are slow balanced motions. In quasigeostrophic theory, which captures the leading-order balance of the slow motions of the primitive equations, the eddy vorticity and eddy temperature forcing contain all the necessary information regarding the forcing of balanced motions.

Following the analogy with QG flow, one need determine only the eddy forcing of potential vorticity in order to capture the tropospheric eddy forcing of the stratospheric long waves. However, the primitive equation model formulation does not allow this directly. The total effective eddy vorticity forcing was derived indirectly by combining the eddy vorticity and eddy temperature forcing fields through a transformation of the Fourier decomposition in Eqs. (4). This has been referred to as transformed Fourier decomposition (TFD) transformation. The TFD transformation was defined in analogy with the well-known transformed Eulerian mean (TEM) transformation. We are unaware of previous use of a formalism like the TFD transformation presented here.

The spatial and temporal characteristics of the total eddy forcing, derived through the TFD transformation, were investigated. The total eddy-forcing field displayed a local maximum near tropopause level. Through forced linear model integrations of the TFD equations it was demonstrated that the vertical structure of the total eddy forcing was most simply described as a compact source near tropopause level. Latitude frequency spectra of the total eddy forcing indicated that both wave-1 and wave-2 were forced by the eddies in a roughly uniform manner over the range of frequencies that had influence on the stratosphere.

The forced linear model experiments revealed that only the low-frequency component of the nonlinear tropospheric forcing is important. For example, it was found that the wave-2 packet organization of the baroclinic eddies was associated with a strong higher-frequency wave-2 forcing. However, the zonal-mean flow that developed in the numerical simulation did not support the upward propagation of such high-frequency wave-2 disturbances. As a consequence, the baroclinic wave packets gave rise to little direct forcing of the stratospheric planetary waves in the numerical simulation. However, they do appear to indirectly force the lower-frequency component of the stratospheric planetary-wave response through the spatial and temporal variability of the packets. (This point is further discussed later in this section).

If the basic-state winds in the lower stratosphere were more intense, as is the case for the observed wintertime SH, the Charney–Drazin theorem (see section 5) suggests the possibility for a more direct connection between the baroclinic wave packets and the stratospheric planetary-wave transience. In section 5c we performed several forced linear model experiments designed to test this possibility. By increasing the zonal-mean zonal wind speed in the lower stratosphere of the forced linear model, it was found that the propagation characteristics

of the zonal mean flow could be changed to allow the upward propagation of the higher-frequency wave-2 disturbances that were forced directly by the packets of baroclinic eddies. These experiments suggest that the higher-frequency wave-2 disturbances observed in the SH wintertime stratosphere (Manney et al. 1991) may be directly forced by packets of baroclinic eddies.

Further nonlinear simulations were undertaken to investigate the relation of stratospheric planetary waves to the variability of the wave packets of baroclinic eddies in the troposphere. It is clear from previous studies of the baroclinic wave packets (e.g., Lee and Held 1993; Esler 1997) that the regularity of the packets depends both on the criticality of the flow and strength of diffusion, such that more regular packets are observed for weaker criticality and stronger diffusion.

A 400-day nonlinear integration was performed in which the order of hyperdiffusion was reduced from ∇^6 to ∇^4, so applying stronger damping on all scales. As expected, the baroclinic wave packets became very regular and displayed a constant wave-2 structure subsequent to the spinup of the forced–dissipative simulation. In this new experiment, the amplitudes of geopotential height fluctuations at 10 mb were reduced by a factor of 2 for wave-1 and a factor of 4 for wave-2. Integrated measures of the 15-day low-pass filtered nonlinear forcing in the troposphere (i.e., that which eliminates the strong high-frequency contribution from the baroclinic wave packets) were also reduced by a factor of 2–3 for both waves-1 and 2. On the other hand, the total unfiltered wave-2 forcing, integrated over the troposphere, was approximately equal to the total wave-2 forcing in the less diffusive simulation, which indicates that the more regular wave packets give rise to even stronger high-frequency wave-2 forcing.

The regularization of the high-frequency baroclinic wave packets in the ∇^4 diffusion experiment seems to have a strong impact on the strength of lower-frequency nonlinear forcing for both waves-1 and 2. This would suggest that it is the asymmetry of the packet structures, or variability in their temporal evolution, that gives rise to the smaller-amplitude low-frequency nonlinear forcing, which is responsible for launching waves that are capable of propagating up into the stratosphere in the numerical simulation.

The results of the present study suggest that the dominant source of planetary-wave variability in the SH wintertime stratosphere is the nonlinear longwave forcing associated with the tropospheric baroclinic eddies. In particular it would seem that the tropospheric forcing is intimately connected to the packet organization of the baroclinic eddies in the troposphere. It would be of considerable interest to compare the stratospheric response in a series of numerical simulations in which the baroclinic wave packets spanned the range from regular to chaotic behavior. The initial indication from this study is that a significant amplification of the low-frequency component of the planetary-wave signal in the stratosphere might be realized if the packets were more variable (as they are in observations of the SH; e.g., Lee and Held 1993).

It has been suggested that some weaker wave-2 events observed in the SH wintertime stratosphere might be due to in situ instability of the stratospheric zonal-mean flow (Manney et al. 1991). An interesting question is whether such in situ instability played a role in the stratospheric planetary-wave variability modeled in the present numerical simulations. The answer appears to be that there was little, if any, in situ instability of the planetary waves in the numerical simulations. This conclusion is primarily based on our ability to perform long integrations of the forced linear model. Had the stratospheric flow been unstable, disturbances would have grown exponentially, rapidly dominating the response, and ultimately causing the linear model integration to terminate prematurely.

The only mechanism that could inhibit the unbounded growth of instability in the linear model is the time variability of the basic state. At certain times the basic-state flow might support baroclinic instability, while at other times baroclinic instability could be suppressed. In this way, linear instability could play a role and remain undetected during the forced linear model integrations.

In order to investigate this possibility, we have undertaken several forced linear model simulations, in addition to those already presented, in which the time evolution of the basic-state flow is allowed only up to a specified time. Subsequently, the flow is held time independent for the remainder of the forced linear model integration and the eddy forcing in the troposphere is smoothly turned off. The time at which the evolution of the basic state is switched off was selected to occur just prior to stratospheric events that displayed the weakest connection to the troposphere (i.e., those events thought to be most possibly associated with in situ instability). In each case, subsequent to the time at which the basic-state evolution was switched off, there was no evidence of instability; stratospheric disturbances simply decayed with time. We conclude, therefore, that in situ instability of the time-evolving, and time-mean, zonal-mean stratospheric flow was not present in the numerical simulation and so did not contribute to the response obtained in the numerical simulation.

Several experiments were undertaken at T21 horizontal resolution employing ∇^6 and ∇^8 horizontal diffusion. At this lower resolution it was found that organization of the baroclinic eddies in the troposphere, as well as the planetary-wave response in the stratosphere, significantly depended on the form and strength of the diffusion employed. These experiments suggest that one should take care in the interpretation of stratospheric variability in low-resolution models, which are unlikely to resolve the tropospheric eddy forcing mechanism properly.

The forced linear model experiments did not require high temporal resolution of the nonlinear eddy-forcing

fields. This suggests the possibility of applying the analysis to observations. One could calculate the nonlinear eddy forcing from observations and integrate the forced linear model in order to identify tropospheric eddy events that influence the stratosphere. More simply, one might even hope that important tropospheric events could be identified directly from the structure of the total eddy forcing (9). This would be equivalent to using Figs. 13a and 13c, which display the temporal and spatial structure of the total eddy forcing, to identify eddy events that influence the stratosphere in the numerical simulation.

However, even though the eddy forcing has been highly simplified in Figs. 13a,c (i.e., it has been reduced to one field and temporally filtered), it does not provide a satisfactory guide for predicting stratospheric planetary-wave events in the numerical simulation. For example, it is not always possible to associate the extrema in the nonlinear forcing of wave-2 displayed in Fig. 13c with the bursts of upward E–P flux in Fig. 5c or with the extrema in wave-2 geopotential heights at 10 mb in Fig. 5a. This difficulty is primarily due to the complex meridional structure of the nonlinear eddy forcing. Figures 13a,c represent the rms amplitude (in latitude) of the nonlinear forcing. Therefore, extrema in Figs. 13a,c are associated with anomalously large fluctuations of eddy forcing of arbitrary meridional structure. It is clear that one would have to undertake a more detailed analysis of the meridional structure associated with tropospheric events that influence the stratosphere. We have not yet attempted a more complex analysis of the meridional structure of the forcing.

One of the most important outstanding issues regarding the eddy-forcing mechanism investigated here is its interaction with other tropospheric sources of planetary waves. Future work should be directed toward understanding this interaction and its effect on the results obtained in this study and is perhaps advisable before attempting further to refine the analysis here, for example, in taking account of the meridional structure of the forcing.

Acknowledgments. The authors thank O. Bühler, G. Esler, and T. G. Shepherd for reading and making helpful comments on the manuscript, and T. G. Shepherd and M. E. McIntyre for helpful discussions. This work received support from the Natural Environment Research Council through the U.K. Universities' Global Atmospheric Modelling Project, in particular through research Grant GST/02/0808.

APPENDIX

Model Details

a. Vertical levels

The model employs a total of $n_F = 30$ ''full'' levels and $n_F - 1$ ''half'' levels (e.g., see Hoskins and Simmons 1975) with $n = n_F$ corresponding to the lowest level in the model. In practice the $n_F - 1$ half levels are specified and the n_F full levels are located equidistantly between half levels (using the fact that the $\sigma = 0$ and $\sigma = 1$ are half levels). The locations of the $n_F - 1$ half levels are given by

$$\sigma_i = \begin{cases} \dfrac{\sigma_{\text{tran}} - \sigma_{\text{min}}}{n_{\text{trop}} - 1}(n_F - 1 - i) + \sigma_{\text{min}}, \\ \qquad n_F - n_{\text{trop}} \le i < n_F - 1 \\ \exp\left[\dfrac{\ln(\sigma_{\text{max}}) - \ln(\sigma_{\text{tran}})}{n_F - n_{\text{trop}} - 1}(n_F - n_{\text{trop}} - i) + \ln(\sigma_{\text{tran}})\right], \\ \qquad 1 < i < n_F - n_{\text{trop}}, \end{cases}$$

where $n_{\text{trop}} = 9$ is the number of levels in the troposphere, which are linearly spaced up to $\sigma_{\text{tran}} = 0.1$, and the lowest and highest half levels are $\sigma_{\text{min}} = 1 - (1 - \sigma_{\text{tran}})/n_{\text{trop}}$ and $\sigma_{\text{max}} = 6.e^{-7}$, respectively. It is also found useful to smooth the transition between linear and logarithmic spacing over a depth of five levels in order to facilitate the elimination of a vertical two-grid wave in the temperature field that is minimized during the balancing procedure used to initialize the model (Hoskins and Simmons 1975).

b. Initial zonal wind

The functional form of the initial zonal wind is

$$U(z, \phi) = G(\phi)[U_{\text{trop}}(z)F_{\text{trop}}(\phi) + U_{\text{strat}}(z)F_{\text{strat}}(\phi)],$$

where

$$U_{\text{trop}}(z) = \begin{cases} \Omega \cdot z, & 0 \le z \le z_t \\ a(z - z_2)^4 + b(z - z_2)^3 & \\ \quad + c(z - z_2)^2 + U_{0t}, & z_t \le z \le z_2 \\ U_{0t}\ \text{sech}^2[(z - z_2)/c_2], & z_2 \le z, \end{cases}$$

$$\Omega = 1.2\frac{U_{0t}}{z_2},$$

$$a = \frac{-3}{(z_t - z_2)^4}U_{0t} + \frac{3}{(z_t - z_2)^4}\Omega z_t - \frac{2}{(z_t - z_2)^3}\Omega,$$

$$b = \frac{8}{(z_t - z_2)^3}U_{0t} - \frac{8}{(z_t - z_2)^3}\Omega z_t + \frac{5}{(z_t - z_2)^2}\Omega,$$

$$c = \frac{-6}{(z_t - z_2)^2}U_{0t} + \frac{6}{(z_t - z_2)^2}\Omega z_t - \frac{3}{(z_t - z_2)}\Omega,$$

$$F_{\text{trop}}(\phi) = \text{sech}\left(\frac{\phi - \phi_2}{b_2}\right),$$

$$U_{\text{strat}}(z) = U_{0s}\,\text{sech}^2\left(\frac{z - z_1}{c_1}\right)\frac{1 + \tanh[(z - z_2)/(z_2 - z_t)]}{2},$$

$$F_{\text{strat}}(\phi) = \text{sech}^2\left(\frac{\phi - \phi_1}{b_1}\right),$$

$$G(\phi) = \tanh\left(\frac{\phi}{5}\right)\tanh\left(\frac{90 - \phi}{5}\right).$$

The tropospheric jet is located at $\phi_2 = 30°$, $z_2 = 12$ km. It has a vertical and meridional half width of $c_2 = 7.5$ km, $b_2 = 12°$, respectively, and a peak wind of $U_{\text{ot}} = 40$ m s^{-1}. Below $z_t = 7.5$ km constant vertical wind shear is imposed. The stratospheric jet is located at $\phi_1 = 50°$, $z_1 = 65$ km. It has a vertical and meridional half width of $c_1 = 34$ km, $b_1 = 20°$, respectively, and a peak wind of $U_{\text{os}} = 62$ m s^{-1}. In the expression for $U_{\text{strat}}(z)$, the factor involving tanh is included to prevent the stratospheric jet from altering the vertical structure of the wind near the surface.

REFERENCES

Andrews, D. G., and M. E. McIntyre, 1976: Planetary waves in horizontal and vertical shear: The generalized Eliassen–Palm relation and the mean zonal acceleration. *J. Atmos. Sci.,* **33,** 2031–2048.

——, and ——, 1978: Generalized Eliassen–Palm and Charney–Drazin theorems for waves on axisymmetric mean flows in compressible atmospheres. *J. Atmos. Sci.,* **35,** 175–185.

——, J. R. Holton, and C. B. Leovy, 1987: *Middle Atmosphere Dynamics.* Academic Press, 489 pp.

Berbery, E. H., and C. S. Vera, 1996: Characteristics of the Southern Hemisphere winter storm track with filtered and unfiltered data. *J. Atmos. Sci.,* **53,** 468–481.

Boyd, J. P., 1976: The nonlinear action of waves with the zonally averaged flow on a spherical earth and the interrelationships of eddy fluxes of energy, heat, and momentum. *J. Atmos. Sci.,* **33,** 2285–2291.

Charney, J. G., and P. G. Drazin, 1961: Propagation of planetary-scale disturbances from the lower into the upper atmosphere. *J. Geophys. Res.,* **66,** 83–109.

Chen, P., and W. A. Robinson, 1992: Propagation of planetary waves between the troposphere and stratosphere. *J. Atmos. Sci.,* **49,** 2533–2545.

Duffy, D. G., 1995: Transient stratospheric planetary waves generated by tropospheric forcing. *J. Atmos. Sci.,* **52,** 3109–3128.

Esler, G, 1997: Wave packets in simple equilibrated baroclinic systems. *J. Atmos. Sci.,* **54,** 2820–284.

Fels, S. F., 1986: Analytic representations of standard atmosphere temperature profiles. *J. Atmos. Sci.,* **43,** 219–221.

Gall, R., R. Blakeslee, and R. C. J. Somerville, 1979a: Baroclinic instability and the selection of the zonal scale of the transient eddies of the middle latitudes. *J. Atmos. Sci.,* **36,** 767–784.

——, ——, and ——, 1979b: Cyclone-scale forcing of ultralong waves. *J. Atmos. Sci.,* **36,** 1692–1698.

Hayashi, Y., and D. G. Golder, 1987: Effects of wave–wave and wave–mean flow interactions on the growth and maintenance of transient planetary waves in the presence of a mean thermal restoring force. *J. Atmos. Sci.,* **44,** 3392–3401.

Hendon, H. H., and D. L. Hartmann, 1985: Variability in a nonlinear model of the atmosphere with zonally symmetric forcing. *J. Atmos. Sci.,* **42,** 2783–2797.

Hoskins, B. J., and A. J. Simmons, 1975: A multi-layer spectral model and the semi-implicit method. *Quart. J. Roy. Meteor. Soc.,* **101,** 637–655.

——, M. E. McIntyre, and A. W. Robertson, 1985: On the use and significance of isentropic potential vorticity maps. *Quart. J. Roy. Meteor. Soc.,* **111,** 877–946.

Kushner, P. J., and T. G. Shepherd, 1995: Wave-activity conservation-laws and stability theorems for semi-geostrophic dynamics. 1. Pseudomomentum-based theory. *J. Fluid Mech.,* **290,** 67–104.

Lee, S., and I. M. Held, 1993: Baroclinic wave packets in models and observations. *J. Atmos. Sci.,* **50,** 1413–1428.

Leovy, C. B., and P. J. Webster, 1976: Stratospheric long waves: Comparison of thermal structure in the Northern and Southern Hemispheres. *J. Atmos. Sci.,* **33,** 1624–1638.

MacVean, M. K., 1985: Long-wave growth by baroclinic processes. *J. Atmos. Sci.,* **42,** 1089–1102.

Manney, G. L., J. D. Farrara, and C. R. Mechoso, 1991: The behavior of wave 2 in the Southern Hemisphere stratosphere during late winter and early spring. *J. Atmos. Sci.,* **48,** 976–998.

McIntyre, M. E., and W. A. Norton, 1990: Dissipative wave-mean interactions and the transport of vorticity or potential vorticity. *J. Fluid Mech.,* **212,** 403–435.

Mechoso, C. R., A. O'Neill, V. D. Pope, and J. D. Farrara, 1988: A study of the stratospheric final warming of 1982 in the Southern Hemisphere. *Quart. J. Roy. Meteor. Soc.,* **114,** 1365–1384.

Randel, W. R., 1987: A study of planetary waves in the southern winter troposphere and stratosphere. Part I: Wave structure and vertical propagation. *J. Atmos. Sci.,* **44,** 917–935.

——, 1992: Global atmospheric circulation statistics, 1000-1mb. NCAR Tech. Note NCAR/TN-366+STR, 256 pp. [Available from UCAR Communications, P.O. Box 3000, Boulder, CO 80307-3000.]

——, D. E. Stevens, and J. L. Stanford, 1987: A study of planetary waves in the Southern winter troposphere and stratosphere. Part II: Life cycles. *J. Atmos. Sci.,* **44,** 936–949.

Simmons, A. J., 1974: Planetary-scale disturbances in the polar winter stratosphere. *Quart. J. Roy. Meteor. Soc.,* **100,** 76–108.

Wyatt, L. R., 1981: Linear and nonlinear baroclinic instability of the Northern Hemisphere winter zonal flow. *J. Atmos. Sci.,* **38,** 2121–2129.

Yamazaki, K., and C. R. Mechoso, 1985: Observations of the final warming in the stratosphere of the Southern Hemisphere during 1979. *J. Atmos. Sci.,* **42,** 1198–1205.

Young, R. E., 1986: Effects of eddy initial conditions on nonlinear forcing of planetary waves by amplifying baroclinic eddies. *J. Atmos. Sci.,* **43,** 3241–3249.

——, and G. L. Villere, 1985: Nonlinear forcing of planetary scale waves by amplifying unstable baroclinic eddies generated in the troposphere. *J. Atmos. Sci.,* **42,** 1991–2006.

——, and H. Houben, 1989: Dynamics of planetary-scale baroclinic waves during Southern Hemisphere winter. *J. Atmos. Sci.,* **46,** 1365–1383.